

# Towards Low-Latency Parallel Readout of Multiple Trapped Ions

Nick Schwegler  
*ETH Zürich*  
Master Thesis

Supervisors:  
Roland Matt  
Dr. Abdulkadir Akin  
Prof. Dr. Jonathan P. Home

October 16, 2018

# Contents

<b>Introduction</b>	<b>3</b>
<b>1 Readout Parameters</b>	<b>5</b>
1.1 $^{40}\text{Ca}^+$ Ion	6
1.2 Optics	7
1.3 Detector	9
1.3.1 EMCCD	10
1.3.2 Comparison between Sensor Technologies	15
1.3.3 Interface	17
1.4 State Analysis	22
1.4.1 State Discrimination Algorithm	22
1.4.2 Hardware for Image Processing	24
<b>2 Implementation of Readout Device</b>	<b>25</b>
2.1 Integration into Control Systems	26
2.2 Frame Grabber and FPGA Selection	28
2.3 FPGA Design and Hardware Architecture	30
2.3.1 Logic Cores	30
2.3.2 Clocking	32
2.3.3 FPGA Simulation	34
2.4 FPGA Hardware Resource Usage	34
2.4.1 Frame Buffer	34
2.4.2 Calibration	35
2.4.3 Image Analysis	36
2.5 Comparison to ARTIQ Sinara Grabber	36
<b>3 Criteria for Readout Devices</b>	<b>38</b>
3.1 Readout Fidelity	38
3.2 State Discrimination Time	43

<b>4 Simulation of Readout Devices</b>	<b>44</b>
4.1 Readout Fidelity . . . . .	45
4.1.1 Spatial Distribution and $\overline{\text{SNR}}$ . . . . .	48
4.1.2 Magnification and ROI Size . . . . .	50
4.1.3 Ion Position Shift . . . . .	52
4.1.4 Ion States and Threshold . . . . .	55
4.1.5 Exposure Time . . . . .	57
4.2 State Discrimination Time . . . . .	58
4.3 Detector Comparison . . . . .	63
<b>Summary and Outlook</b>	<b>67</b>

# Introduction

Qubit readout is a crucial part of quantum information processing. To determine the result of a quantum algorithm [1] or implement Quantum Error Correction (QEC) [2, 3], single-shot readout is an essential tool. Multiple trapped ions in linear chains can be used for universal quantum computation [4] or quantum simulation [5]. Further, quantum simulations can also be performed with 2D ion crystals [6] and neutral atoms [7]. In all of these systems, state discrimination is achieved by detection of optical fluorescence. High-fidelity readout is required to reach the threshold for fault tolerant quantum computation [8]. Often, this threshold is stated with infidelities lower than  $10^{-4}$  per single shot readout operation [9]. Most QEC codes rely on real time feedback based on error syndrome extraction by measurement of ancilla qubits [10]. The fidelity and duration of ancilla readout limits the overall fidelity of such algorithms. Hence, real time state detection with minimal latency is required. For single ions, readout has been realized with high fidelities and low latencies using a Photo-Multiplier-Tube (PMT) [11]. In a scalable architecture with many qubits, parallel readout offers a great speed up compared to serial readout. Detectors with spatial resolution are required to perform parallel readout of multiple qubits, but face the issue of optical cross talk between neighboring ions that reduces readout fidelity. Parallel readout of trapped ions has been achieved using multi-channel PMT arrays [4, 12] with low latency but limited fidelity. High-fidelity parallel readout has been performed with Electron-Multiplying Charge Coupled Devices (EMCCD) [13, 14], but latencies are typically high since images are post-processed on a PC.

In this work, I explore the possibility of using a readout device consisting of a commercially available EMCCD or CMOS (complementary metal-oxide-semiconductor) camera in combination with image processing on a Field-Programmable Gate Array (FPGA). I conclude that, in contrast to other approaches, this offers a scalable solution towards low-latency and high-fidelity parallel ion readout. Our readout device acts as a standalone device

complementary to existing experiment control systems. A typical experiment setup of ion traps for quantum information processing consists of the following components [15]: In Paul traps, ions are confined in linear chains using time-varying electrical fields. Lasers are aimed at the trap sites to cool the motion of the ions and manipulate their internal (electronic) states. Electronic energy levels are used to define qubits, initialized by optical pumping. Single qubit gates can be realized by coupling to electro-magnetic fields like lasers or microwave radiation. Interactions between qubits for multi-qubit gates are mediated by additional use of the common motion of the ion chain. Projective measurement of internal states is achieved by driving electronic cycling transitions that induce state-dependent fluorescence, which is recorded by detectors. A classical experiment control system is used to control laser systems and the trap in real time. In our lab, we have an existing setup that uses a fast CPU interfacing an FPGA that implements automated calibration, measurement sequences, and feedback with low latencies [16]. As a proof of principle for camera-based readout with low latencies, I interface an EMCCD camera with an FPGA and verify an FPGA implementation of a fast state discrimination algorithm. A tool is developed to simulate the readout and noise characteristics of EMCCDs and CMOS. Using these simulations, I conclude that with our EMCCD-based readout device we can achieve parallel readout of up to 60 bright ions in a linear chain with an upper-bound infidelity of  $10^{-4}$  in 225  $\mu\text{s}$ .

The thesis has the following outline: First, I discuss the experimental parameters that are relevant for readout of trapped ions in Chapter 1. In Chapter 2, I explain the technical details of our FPGA implementation performing the state analysis. I introduce the readout fidelity and state discrimination time as a measure for the quality of a readout device in Chapter 3. In Chapter 4, I simulate our EMCCD-based readout device and predict its performance. I further compare EMCCD to CMOS and multi-channel PMT detectors and discuss their suitability for parallel readout.

# Chapter 1

## Readout Parameters

In this chapter, I give a detailed description of experimental parameters which are relevant for the readout in ion-trap experiments. Based on typical setups in our labs [17], I present an effort towards low-latency parallel readout of ions using EMCCDs and FPGAs. The parameters influence the quality and speed of our readout device discussed in Chapter 3. The formulas derived and referenced in this chapter are used for numerical simulations in Chapter 4, with values presented in Table 4.1 and 4.2.

The structure of this chapter follows the light emitted by  $^{40}\text{Ca}^+$  ions which is turned into digital signals in a detector and used to determine the ion states. I will describe each relevant element from the atom, imaging system, detector, and state analysis to quantitatively understand this process. The spatial distribution of ion signals on the detector is of particular interest for parallel readout. Due to the diffraction limit of the imaging system, the spatial distributions from multiple ions in a string overlap. This optical cross talk poses a challenge for parallel readout since it reduces the ion readout fidelity depending on the state of its neighbors, see Section 4.1. To quantify the single-shot readout fidelity, the detector signal needs to be characterized shot-by-shot. For this, the count distributions for EMCCD, PMT and CMOS sensors needs to be considered. Since readout speed is crucial for measurement-based feedback loops, I investigate the camera readout time of an EMCCD. It is determined by the clocked charge transport on the EMCCD sensor. Further, I examine different camera interfaces and conclude that the only interface which can meet the requirements for low-latency applications is Camera Link. I argue that image-based state analysis is best carried out on FPGAs, since they are orders of magnitude faster than serial processors on PCs.

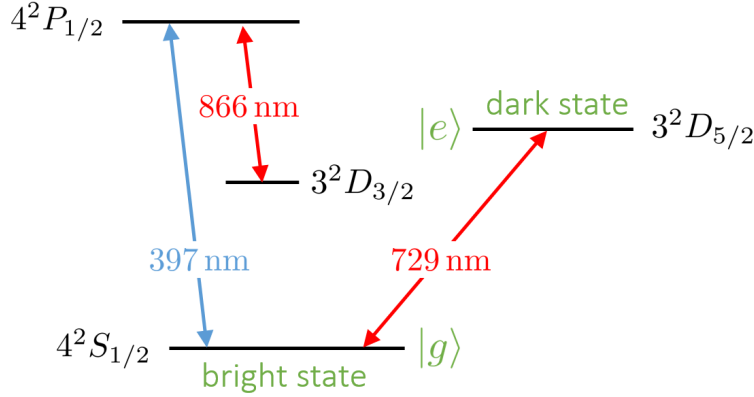


Figure 1.1:  $^{40}\text{Ca}^+$  level diagram, sub-levels are not drawn for simplicity. Shown are the lowest energy levels of the valence electron involved in definition and readout of the optical qubit. The excited state  $|e\rangle$  remains dark during readout, hence it is referred to as “dark state”, while the ground state  $|g\rangle$  is bright and referred to as “bright state”.

## 1.1 $^{40}\text{Ca}^+$ Ion

The atomic level structure of ions can be used to define qubits. Qubit readout can be performed by state-dependent fluorescence detection. In the following, I explain the standard readout scheme used with calcium ions  $^{40}\text{Ca}^+$  [15, 18] as an example and quantify the rate of ion fluorescence.

Since  $^{40}\text{Ca}^+$  has no nuclear spin, the atomic energy levels show no hyperfine splitting and are well described by the total angular momentum  $J = S + L$ . The eigenstates are given by LS-multiplets with standard notation  $n^{2S+1}L_J$ , where  $n$  is the principal quantum number,  $S = 1/2$  the total spin for a single valence electron and  $L$  the orbital angular momentum.

Figure 1.1 shows the energy levels of the valence electron. The “optical qubit” is encoded in any of the  $D_{5/2}$  levels (excited state) and  $S_{1/2}$  levels (ground state). The excited state is meta-stable with a natural lifetime of  $\sim 1\text{ s}^1$ . A resonant laser on the optical quadrupole transition  $S \leftrightarrow D$  at 729 nm can be used for coherent manipulation of the qubit.

The  $S \leftrightarrow P$  transition at 397 nm is dipole-allowed and the  $P_{1/2}$  level

<sup>1</sup>A longer lived “microwave qubit” can be defined in the two energy levels of  $S_{1/2}$ , which are Zeeman split when an external magnetic field is applied. Readout of the microwave qubit can be achieved using the standard readout scheme by first mapping it to the optical qubit with state-selective shelving.

decays quickly with a natural lifetime of  $\sim 7.7$  ns. A “readout” laser on resonance with this transition induces natural fluorescence for the ground state, whereas the excited state appears dark. The  $S \leftrightarrow P$  cycle is not completely closed since there is some leakage to the  $D_{3/2}$  level. Therefore, a 866 nm “repump” laser is required. The state-dependent fluorescence can be used to discriminate the qubit states and is described in [13] and Appendix B of [19]. The fluorescence rate  $R_B$  of the bright state is given by

$$R_B = A_{21}n_2, \quad (1.1)$$

where  $A_{21}$  is the Einstein coefficient for the  $S \leftrightarrow P$  transition and  $n_2$  the population of the  $P_{1/2}$  level. The population can be obtained by solving the rate equations for the three levels involved in readout. Assuming that the repump laser is driven at high intensity, and that the readout laser is close to resonance, the population only depends on the intensity of the readout laser  $I$  and is given by:

$$n_2 = \frac{(I/I_{\text{sat}})}{1 + 4(I/I_{\text{sat}})}, \quad (1.2)$$

where  $I_{\text{sat}}$  is the laser saturation intensity to reach equilibrium between spontaneous and stimulated emission for the  $S \leftrightarrow P$  transition. This model assumes linearly polarized lasers and ignores coherent effects.

## 1.2 Optics

Imaging system are used to collect ion fluorescence. Due to the diffraction limit, the ions exhibit broad spatial features on the image plane. The overlap of the spatial distributions is problematic for parallel readout since it causes optical cross talk. In the following, I provide the spatial distributions of ion images and scattered laser light. In Chapter 3.1, they are used to characterize the contribution of ion signal, optical cross talk and background to the mean photon number incident on a pixel.

The total collection efficiency of the imaging setup  $\eta$  is defined as the ratio of the amount of fluorescence light reaching the image plane and the total amount of fluorescence light emitted by the ions. The efficiency is mainly limited by the small solid angle coverage of the objective.

To maximize the coverage, fluorescence light is collected with a high numerical aperture objective. A single lens setup can be used [17], but more complicated multi-lens systems [13] allow to change the apparent size of

objects imaged onto the detector<sup>2</sup>. The magnification  $M$  is defined as the ratio between the size of an object in the object plane and its apparent size in the image plane.

The derivations of the formulas stated in the following can be found in Section 10.2.5 and 11.3.1 in [20]. Due to the diffraction limit given by the imaging system, the image of an ion on the detector is spread out. The ion's spatial distribution in the image plane is given by the Point Spread Function (PSF) magnified by  $M$ . The PSF of a diffraction-limited system is calculated by the squared modulus of the Fourier transform of the aperture. For a circular aperture representing the objective, the PSF of ion  $k$  is given by the Airy function:

$$I_k(r_k(x, y)) = \left( \frac{2J_1(r)}{r} \right)^2, \quad (1.3)$$

with

$$r_k(x, y) = \frac{2\pi \text{NA} \sqrt{\left| \frac{x-x_k}{M} \right|^2 + \left| \frac{y-y_k}{M} \right|^2}}{\lambda \sqrt{1 - \text{NA}^2}}, \quad (1.4)$$

where  $x$  and  $y$  are coordinates in the image plane,  $x_k$  and  $y_k$  the position of ion  $k$  in the image plane, NA the numerical aperture of the imaging setup,  $\lambda$  the fluorescence wavelength and  $J_n(k)$  the Bessel function of the  $n$ -th kind.

The spot size of an ion on the detector for a diffraction limited system is characterized by the Airy radius  $R_{\text{Airy}}$ , which is defined as distance from the center to the first minimum of the Airy function

$$R_{\text{Airy}} = 1.22\lambda M \frac{\sqrt{1 - \text{NA}^2}}{2\text{NA}}. \quad (1.5)$$

The spot radius produced by a real imaging system is usually larger than the Airy radius due to imperfections of the lenses and misalignment. For the spot size only, I approximate the real imaging setup by a diffraction limited system with a lower effective numerical aperture, such that resulting Airy radius is equal to the measured spot radius. I keep using the collection efficiency of the real imaging system, independent of the effective numerical aperture.

Due to the ion's spatial distribution on the detector, only a fraction of the ion fluorescence is incident on a particular pixel. I denote the contribution

---

<sup>2</sup>In a setup consisting of two thin lenses for example, the first lens can be used to collimate light, which can then be focused down by a secondary lens onto the detector. By varying the focal length of the secondary lens and its distance to the primary lens, the magnification can be changed, see Section 5.2.3 in [20]

from ion  $k$  to a detector with dimension  $P_x$  and  $P_y$  (e.g. pixel  $ij$ ) by the weight  $w_k^{ij}$ . I calculate it by integration of the PSF over the detector area in the image plane

$$w_k^{ij} = C \int_0^{P_x} \int_0^{P_y} I_k(x, y) dx dy. \quad (1.6)$$

I normalize the weight such that a detector of infinite size has weight 1. This rescaling ensures that the total amount of fluorescence rate reaching the image plane is maintained and given by  $R_B \eta$ . For the Airy function, the norm is given by

$$C^{-1} = \int_{-\infty}^{\infty} \int_{-\infty}^{\infty} I(x, y) dx dy = 2\lambda^2 M^2 \frac{(1 - \text{NA}^2)}{2\pi \text{NA}^2}. \quad (1.7)$$

Not only the ions, but also laser light that is scattered at the trap electrodes is imaged onto the detector. It depends strongly on the trap architecture and contributes to the background signal. Since the detector only needs to be sensitive to the frequency of fluorescence light for readout, any reflections from other frequencies (e.g. repump laser) can be filtered out.

I assume that the intensity of scattered light from the readout laser  $I_L = R_L \hbar \omega$  is uniform in the area around the ions in the object plane. Thus its spatial distribution is uniform with value 1. The contribution to a detector with dimension  $P_x$  and  $P_y$  is given by the weight  $u^{ij}$ . It is the integral of the uniform spatial distribution over the detector area and given by

$$u^{ij} = \frac{1}{M^2} \int_0^{P_x} \int_0^{P_y} 1 dx dy = \frac{P_x P_y}{M^2}, \quad (1.8)$$

where the rescaling factor  $1/M^2$  comes from the fact that the intensity of scattered laser light is constant in the object plane for  $M = 1$ .

### 1.3 Detector

The fluorescence light captured by the imaging system is registered by detectors. In this section, I focus on EMCCD cameras, but also compare it to other sensors technologies. Understanding the working principle of sensors allows us to simulate the detection process and explore their limitations in both quality and speed in Chapter 4.

For all detectors, the detection process is based on converting photons to electrons via the photoelectric effect. This conversion happens with a certain probability, characterized by the quantum efficiency  $Q$  of the detector.

The quantum efficiency generally depends on the frequency of incident light. Including calcium, all ions suitable for trapped ion quantum information experiments have similar cyclic readout schemes with fluorescence light in the UV to blue region from 150 to 450 nm<sup>3</sup>.

### 1.3.1 EMCCD

In the following, I explain the sensor architecture of Electron-Multiplying Charge Coupled Devices (EMCCD). Due to their sensor structure, EMCCDs exhibit both benefits and disadvantages. The relevant noise sources in EMCCD are internal Clock Induce Charge (CIC) noise, readout noise, which can be suppressed by electron multiplication, and excess noise, which arises due to the probabilistic gain process. The shot-by-shot signal is characterized by the pixel count distributions taking into account the EMCCD noise properties. As an approximation, I use the Poisson-Gamma-Normal (PGN) model, which allows for an efficient numerical implementation of the distributions. Since low-latency is a main design criteria, the camera readout speed is crucial. The camera readout time of a Frame Transfer (FT) EMCCD is limited by an analog bottleneck that requires all electrons to be transported from the image area to the Analog-to-Digital Converter (ADC) by a clocked process.

#### Sensor Architecture

In general, Charge Coupled Devices (CCD) control the movement of electrical charge by modifying potential wells created with gate electrodes. They are most commonly used for digital imaging. Electron multiplication (EM) CCDs [21] are a special type of CCDs that reduce readout noise, see below.

Photons are converted to electrons during the exposure and collected in the image area. They are then transported from the image area to a readout zone, where they are converted to digital values. The light-sensitive image area consists of pixels in either a one dimensional array (line sensor)<sup>4</sup> or in a two dimensional array (area sensor). This gives EMCCD cameras spatial resolution. Most EMCCD cameras on the market are Frame Transfer (FT), see Fig. 1.2. They feature a second “storage” area of the same size as the image area. This enables the implementation of an electronic shutter to end

---

<sup>3</sup>See <http://iontrap.umd.edu/resources-2/periodic-table/> for a compilation of different ions and their level structure.

<sup>4</sup>Line sensors tend to have lower readout times. However, I don’t consider them in this project, since EMCCD line sensors are not available on the market at the time of writing. CCD and CMOS line sensors are typically too noisy for ion readout.

the exposure by quickly moving the electrons from the image area to the storage area.

I now discuss the different noise sources in EMCCDs. Electrons are converted to voltage with a charge amplifier. This process is generally noisy and gives some uncertainty in the number of electrons. I refer to it as **readout noise**  $\sigma$  in the following. The voltage is then digitalized in an Analog-to-Digital Converter (ADC). Readout noise in CCD cameras is on the order of a few electrons per pixel. To make a camera that is not limited by this, the readout noise is effectively reduced by adding a large number of EM registers before the ADC. In each of these “gain registers”, the electrons are multiplied by impact ionization, producing an electron avalanche. The EM gain factor  $G$  is defined as the mean number of output electrons after the gain stages for a single input electron. Typically, EM gains of up to 5000 can be achieved. The amplifier readout noise is superimposed onto thousands of electrons after the gain registers, rather than single electrons before. The effective readout noise is given by

$$\sigma_{\text{eff}} = \frac{\sigma}{G}. \quad (1.9)$$

This gain process from impact ionization is stochastic in each gain register, resulting in a probabilistic distribution of output electrons. This uncertainty in the number of output electrons given the input electrons introduces an additional noise factor in EMCCDs, which I refer to as **excess noise**.

EMCCD cameras have two additional internal noise sources. Both of them produce unwanted electrons before the gain registers that do not stem from photons and add to the background signal. I do not consider spurious charge at or after the gain stages in my models. Caused by a similar effect that provides the gain for electron multiplication, Clock Induced Charges (CIC) can be produced when photoelectrons are moved from one pixel to another. The **CIC noise** is independent of exposure time and is introduced for each pixel as  $\lambda_{\text{CIC}}$ . Electrons can also be created from thermal energy within the CCD structure itself. Thermal dark counts increase with exposure time. Since EMCCD sensors are actively cooled and typical exposure times for ion readout short, the contribution from thermal dark currents is negligible.

Due to the EMCCD sensor architecture, all pixels pass through the same amplifier and ADC. This has a negative effect since it forms an analog bottleneck that limits the readout speed, but it also guarantees almost perfect uniformity over the whole sensor. To achieve fast readout, the ADC needs to run at higher frequencies ( $f_h$ ), resulting in higher readout noise, which

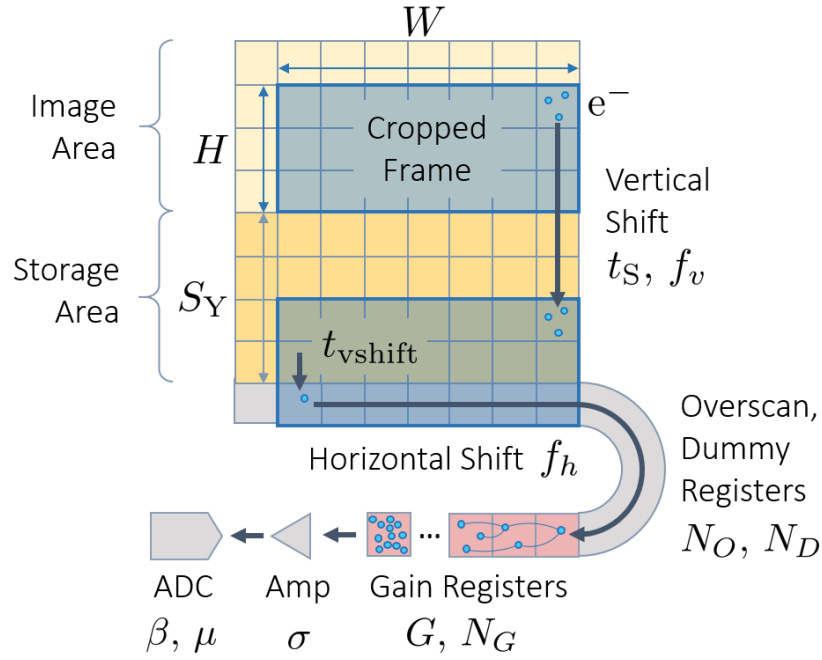


Figure 1.2: Architecture of a Frame Transfer EMCCD camera. Shown is the path of signal from photoelectrons to digital values. This process involves the relevant noise sources and gives rise to the camera readout time. Photoelectrons are accumulated in the cropped frame region ( $W \times H$  pixels) during the exposure. They are vertically shifted down by the electronic shutter from the light-sensitive image area to the bottom of the light-proof storage area. From there, each line is shifted vertically once, and horizontally through the overscan, dummy and gain registers, where the electrons are multiplied. Finally, electrons are converted to digital values at the amplifier (Amp) and ADC. Labeled are all the parameters relevant for the readout fidelity and state discrimination time. To illustrate the electron multiplication and charge transport, some exemplary electrons are shown as blue dots.

can be compensated by high gains. The ADC introduces a conversion factor  $\beta$  when translating electrons to counts. To ensure that counts are always positive, an offset  $\mu$  is added. Both  $\beta$  and  $\mu$  are irrelevant for the readout fidelity.

### Pixel Count Distribution

Here I introduce a mathematical model for the count distributions of the pixels in an EMCCD. It incorporates all noise sources discussed in Section 1.3.1 and can be used to simulate the shot-by-shot behavior of EMCCDs sensors.

The probability density function of counts  $P(n|\lambda)$  for each pixel depends on the mean photon number  $\lambda$  and sensor noise properties. A high-gain approximation is given by the Poisson-Gamma-Normal (**PGN**) model. This is a good approximation, since EMCCD usually run at high gains to reduce readout noise. In the following, I give a short summary of the PGN model derived in [22]. It is based on the following three distributions:

Firstly, a **P**oisson distribution with mean (and variance)  $\lambda = Q\lambda_{\text{inc}} + \lambda_{\text{CIC}}$ , where  $Q$  is the quantum efficiency of the detector,  $\lambda_{\text{inc}}$  the mean number of incident photons and  $\lambda_{\text{CIC}}$  the CIC. Both the photons arriving at the detector and CIC creation are probabilistic and governed by Poissonian statistics. The total number of electrons before the gain registers is given as the convolution between the two, which is a Poissonian with added mean. The variance is referred to as “shot noise”.

Secondly, a **G**amma distribution that models the stochastic electron multiplication in the gain registers. Starting from  $\lambda$  input electrons, its expectation value is given by  $\lambda G$ . The variance is  $2G^2\lambda$ , which represents the excess noise.

Lastly, a **N**ormal distribution with mean  $\mu$  and variance  $\sigma^2$  that describes the uncertainty introduced by the readout noise.

The total probability density function is given by a composition of the Poisson and Gamma distribution and an approximated convolution with the Normal distribution. It results in the following formula:

$$P^{\text{PGN}}(n|\lambda) = \begin{cases} \frac{1}{\sqrt{2\pi\sigma}} \exp\left(-\lambda - \frac{(\beta(n-\mu))^2}{2\sigma^2}\right) & n - \mu \leq 0 \\ \frac{1}{\sqrt{2\pi\sigma}} \exp\left(-\lambda - \frac{(\beta(n-\mu))^2}{2\sigma^2}\right) & n - \mu > 0 \\ \quad + \frac{2}{G} F_\chi(2\lambda; 4, 2\beta(n-\mu)/G) & \end{cases}, \quad (1.10)$$

where  $F_\chi$  is the non-central  $\chi^2$  distribution for  $2\lambda$  with 4 degrees of freedom and non-centrality parameter  $2\beta(n - \mu)/G$ . By linearity of the mean and the Bienaymé formula [23], the PGN model has mean  $\lambda G + \mu$  and variance  $2G^2\lambda + \sigma^2$ .

## Readout Time

In the following, I derive a formula for the camera readout time of a FT EMCCD. It can be used to estimate the readout time of a camera based on the sensor specifications. The proposed model is verified with a measurement of the *Andor iXon 888* camera in Section 4.2. I conclude that EMCCD readout times depend on the dimension, orientation and position of the cropped frame on the sensor.

I define the detector readout time as the time after the exposure until the last bit of information is transferred to the state analysis hardware. For a FT EMCCD, it is limited by an analog bottleneck and determined by the time required to transport charges from the image area to the readout zone, see Fig. 1.2. This process is clocked, hence the transport time is given by the clock frequencies and number of required shifts. Cameras have the option to only read out a small part (“crop”) of the full frame. This following model assumes that the cropped frame is placed at the bottom corner of the image area closest to the readout zone as illustrated in Fig. 1.2. Any other position would require further shifts and add more delay. Depending on the width  $W$  and height  $H$  of the cropped frame, the camera readout time is given by

$$\begin{aligned}
 t_{\text{read}}(H, W) \approx & t_S + \frac{1}{f_v} S_Y \\
 & + \frac{1}{f_h} (N_D + N_G) \\
 & + H \left( t_{\text{vshift}} + (W + N_O) \frac{1}{f_h} \right),
 \end{aligned} \tag{1.11}$$

where  $t_S$  is a delay before shifting the image through the storage area,  $S_Y$  the height of the storage area,  $N_D$  and  $N_G$  the number of dummy and gain registers,  $t_{\text{vshift}}$  the time for a single vertical line shift during line readout,  $N_O$  the number of overscan pixels,  $f_v$  and  $f_h$  the vertical and horizontal shift frequency.

The vertical shift through the storage area is delayed and only happens once at the beginning of the readout. The horizontal shift through the dummy and gain registers represents a constant offset. The line readout

is repeated for the cropped frame height. The camera readout time depends linearly on the cropped frame size ( $H \times W$  pixels). The partial derivatives for constant widths and heights are given by

$$\left. \frac{\partial t_{\text{read}}(H, W)}{\partial H} \right|_W = t_{\text{vshift}} + (W + N_O) \frac{1}{f_h} \quad (1.12)$$

and

$$\left. \frac{\partial t_{\text{read}}(H, W)}{\partial W} \right|_H = H \left( \frac{1}{f_h} \right). \quad (1.13)$$

For reading out lines at constant height there is no additional shift time. This means reading out one line is always faster than reading out one row due to the EMCCD sensor architecture. Therefore, reading out rectangles with dimensions  $W > H$  is faster. I only consider cropped frames with optimal position and orientation in the following.

### 1.3.2 Comparison between Sensor Technologies

In this subsection, I compare EMCCD sensors to two other types of detectors. Firstly, Multi-channel Photo-Multiplier-Tubes (PMTs), which have already been used for parallel readout of multiple ions [4, 12]. Secondly, CMOS (complementary metal-oxide-semiconductor) sensors, which are a promising candidate for parallel ion readout due to their high sensitivity and potentially fast camera readout. Based on the corresponding sensor technology, I describe how the sensors can be simulated with pixel count distributions. This knowledge is used in Section 4.3 to evaluate and compare the performance of EMCCD, multi-channel PMT and CMOS for parallel ion readout. Typical specifications of state-of-the-art EMCCD, multi-channel PMT and CMOS can be found in Table 4.2.

#### Multi-Channel PMT

The current standard detector for single ion readout is the Photomultiplier Tube (PMT) [11]. Due to the lack of spatial resolution, PMTs are limited to serial ion readout. By expanding the structure, it is possible to build multi-channel PMT array that can achieve parallel ion readout with multiple PMT pixels [4, 12].

I now briefly discuss how multi-channel PMTs work<sup>5</sup>. On each PMT

---

<sup>5</sup>See [https://www.hamamatsu.com/resources/pdf/etd/PMT\\_handbook\\_v3aE.pdf](https://www.hamamatsu.com/resources/pdf/etd/PMT_handbook_v3aE.pdf) and [https://www.hamamatsu.com/resources/pdf/etd/LINEAR\\_PMT\\_TPMH1325E.pdf](https://www.hamamatsu.com/resources/pdf/etd/LINEAR_PMT_TPMH1325E.pdf) for details.

pixel, a photon is converted to an electron in a photocathode. The photoelectron is multiplied by means of secondary electron emission at many dynodes, resulting in an electron avalanche. The output charge is converted to voltage using an amplifier, which is then compared to a threshold. Whenever the threshold is reached, the PMT pixel has detected a photon and sends out a pulse with very low latency. This enables a high resolution in time with negligible readout times. The readout is done parallel for all pixels using many channels. The exposure time is the time period during which photons are counted.

The gain process in PMT pixels is stochastic and similar to the electron multiplication in an EMCCD, with the difference that it only ever has one input electron. This is because PMT pixels can detect and process single photons at a time, whereas EMCCDs accumulate many electrons during exposure and process them collectively. However, multi-channel PMTs suffer from significant electronic cross talk on the order of one percent. The electron multiplication process is violent involving high voltages and neighboring dynodes are in close proximity. This means electrons in the multiplication stage of one pixel can escape and jump to the multiplication stage of another pixel. There they launch an additional electron avalanche, which can er the threshold and give unwanted counts. In EMCCDs, electronic cross talk is not an issue, since only a single multiplication stage is used.

Multi-channel PMTs have no internal noise sources and are limited only by the shot noise of the incident photons. The probability density function describing the PMT pixel counts is a Poissonian with mean  $Q\lambda_{inc}$ .

Compared to EMCCDs, the PMT pixel area is orders of magnitudes larger. There are gaps between the pixels, which are of the same order of magnitude as the pixel width. This limits the spatial resolution of multi-channel PMTs and requires high magnifications to image linear ion chains.

## CMOS

CMOS sensors [24] are an alternative to CCDs. They are integrated circuit active-pixel sensors and manufactured using Complementary Metal-Oxide-Semiconductor (CMOS) technology. Unlike a CCD, which is based on electron transport and serial pixel readout, each pixel in a CMOS contains its own amplifier and ADC. The photoelectrons are read out in parallel within each pixel and the resulting pixel values are collected in a fast digital bus. This gets rid of the analog bottleneck and generally allows for higher readout speeds in CMOS.

However, CMOS suffer from a low pixel uniformity [25, 26]. Due to

fabrication imperfections of the amplifiers, each pixel has a different readout noise  $\sigma_{ij}$ . The readout noise follows a specific pixel distribution that is often only characterized by its RMS value  $\sigma_{\text{rms}}$ . Some pixels perform worse than the RMS value and are called “hotpixels”. Since there is no gain process, CMOS are typically readout noise limited.

The noise characteristics of the count distribution  $P_{ij}(n|\lambda)$  is different for each pixel ( $ij$ ). It is given by the convolution between a Poissonian with mean  $Q\lambda_{inc}$  and a Normal distribution with mean  $\mu$  and variance  $\sigma_{ij}^2$ . The Modified Poissonian Model (MPM) approximates the convolution [27].  $P_{ij}^{\text{MPM}}(n|\lambda)$  is a Poissonian with mean  $Q\lambda + \sigma_{ij}^2$  and index  $n + \sigma_{ij}^2$ , which is analytically extended to be continuous:

$$P_{ij}^{\text{MPM}}(n|\lambda) = C \times \frac{(\lambda + \sigma_{ij}^2)^{\beta(n-\mu) + \sigma_{ij}^2}}{\Gamma(\beta(n-\mu) + \sigma_{ij}^2 + 1)} e^{-\lambda - \sigma_{ij}^2}, \quad (1.14)$$

where  $\Gamma(x)$  is the Gamma function and  $C$  used to normalize the count distribution.

### 1.3.3 Interface

To determine the state of ions, detectors that register the ion fluorescence need to be interfaced with the state analysis hardware described in Section 1.4. Spatially resolved detectors used for parallel ion readout transmit digital data in form of arrays. In our readout device, cameras with area sensors use fast serial interfaces to transmit images, which are captured by a frame grabber and processed in an FPGA, see Chapter 2

In this subsection, I explain the “Camera Link” interface used by our EMCCD camera and compare it to other camera interfaces. I conclude that Camera Link is the only suitable interface for low-latency FPGA-based image processing. It is well-established in the machine vision industry and is used by many cameras on the market.

#### Camera Link Interface

Camera Link is a serial communication protocol standard<sup>6</sup> developed for industrial machine vision cameras. The protocol describes the transfer of a 2D data array, for example pixels in an image. As an example, Fig. 1.3 shows the timing diagram for the transfer of the pixel matrix in (1.15). Each image

---

<sup>6</sup>The specifications can be found on <http://www.imagelabs.com/wp-content/uploads/2010/10/CameraLink5.pdf>

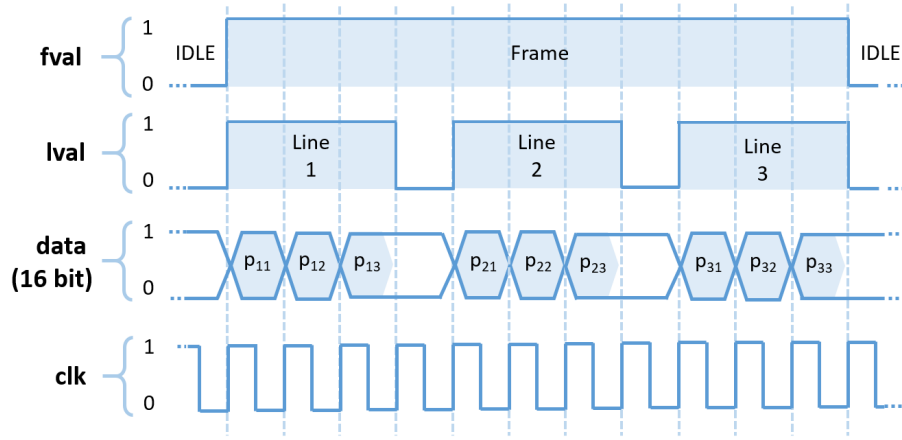


Figure 1.3: Example timing diagram of the Camera Link protocol for a  $3 \times 3$  image array (1.15) without additional serialization of the pixel values. Frame valid (fval) and line valid (lval) describe the start and end of a frame or line respectively. The pixels are transmitted in series, from top left to bottom right. For the cameras considered in this project, the pixel values are usually described by 16 bits.

is sent line by line, starting from the top, and pixel by pixel, starting from the left. A frame starts when frame valid (fval) is high, a line starts when line valid (lval) is high. When both fval and lval are high, the pixels in a line are transmitted. The transmission happens with no overhead in parallel to the serial EMCCD pixel readout described in subsection 1.3.1 and starts as soon as the first pixel is read out in the ADC.

$$\begin{pmatrix} p_{11} & p_{12} & p_{13} \\ p_{21} & p_{22} & p_{23} \\ p_{31} & p_{32} & p_{33} \end{pmatrix} \quad (1.15)$$

Additionally, the data (including fval and lval) is serialized in the transmitter (camera) and deserialized in the receiver (frame grabber) to reduce the size of the connector and cable. The physical layer is based on the 28-bit “Channel Link” chip family DS90CR28x<sup>7</sup> by National Semiconductor. It uses a driver and receiver pair consisting of 4 data LVDS pairs and one clock LVDS pair. The data serialization is done 7:1, meaning in a single clock cycle  $4 \times 7 = 28$  bits can be transmitted. The timing diagram for the transmission

<sup>7</sup><http://www.ti.com/lit/ug/snla167/snla167.pdf>

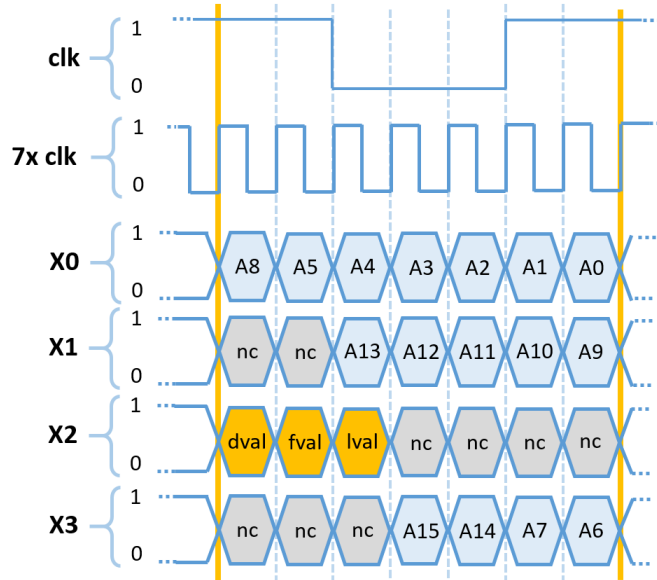


Figure 1.4: Timing diagram of 7:1 serialization on the physical layer. Shown is the transmission of a single pixel (A0-A15 in blue). This 16 bit Base configuration only uses a single Channel Link chip (Port X). There are 9 unused data slots in grey (not connected - nc). In theory, a total of 24 data bits can be transmitted per cycle. Note that data valid (dval) is optional and not implemented in many cameras. The clock has duty cycle 4:3, the falling edge is after the second bit.

of a single pixel can be found in Fig. 1.4.

Camera Link comes in three different configurations: Base, Medium and Full, see Fig. 1.5. Base only uses a single Channel Link chip with a single connector, while Medium and Full use two connectors with two or three chips. The more transceiver chips are used, the higher bandwidth can be achieved. For EMCCDs, the bandwidth of Base configurations already suffices: With up to 85 MHz, the Camera Link interface can run faster than the EMCCD pixel readout and pixel depths are usually lower than 24 bits. The connectors used with Camera Link are 26-pin Mini Delta Ribbon (MDR) or in a smaller variant 26-pin Shrunk Delta Ribbon (SDR). The maximum supported cable length is around 10 meters, or 25 meters with a repeater.

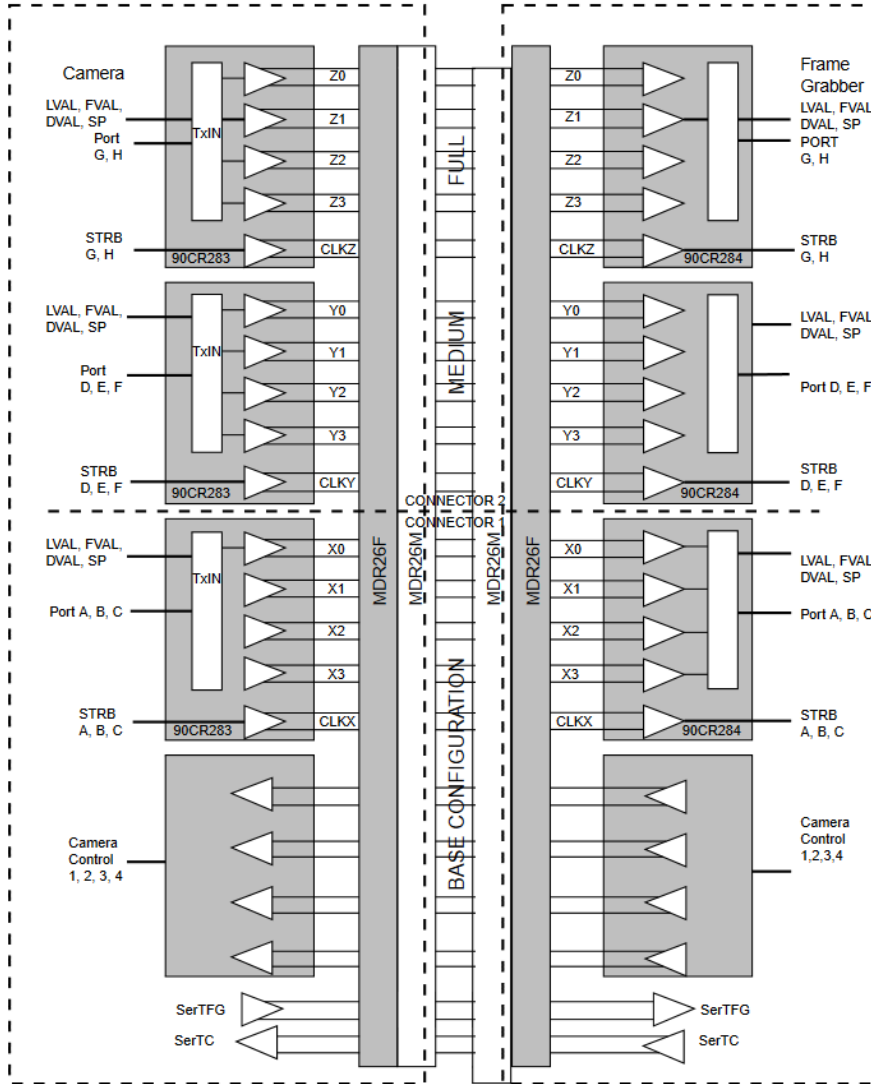


Figure 1.5: Comparison between Base, Medium and Full Camera Link configurations. The data is transferred from left (camera) to right (frame grabber). There are two physical connectors that carry two transceiver chips each (top and bottom). Base configuration uses only port X, Medium X and Y, and Full X, Y and Z. Additionally, there is a Camera Control transceiver that can be used to control the camera. Note that this channel is typically not used, instead the two connections SerTFG (“Serial To Frame Grabber”) and SerTC (“Serial To Camera”) are used for asynchronous serial communication.

Interface	<b>FireWire</b>	<b>USB</b>	<b>GigE</b>	<b>Camera Link</b>
Variant	<i>IEEE 1394B</i>	<i>USB 3.0</i>	<i>10 GigE</i>	<i>Full, 85 MHz</i>
Bandwidth	1.6 Gbps	5 Gbps	10 Gbps	6.1 Gbps
Cable length	4.5 m	5 m	100 m	25 m
Topology	Daisy chain	Point-to-Point, tiered-star	Point-to-Point, Network	Point-to-Point
Format	Packet-based	Packet-based	Packet-based	Parallel
Est. latency	125 $\mu$ s	20 ms	10 $\mu$ s	$\sim$ ns
Frame grabber	PC	PC	PC	FPGA
Robustness	Error detection	Data re-transmission	Data re-transmission	-
Camera control	Full-duplex	Full-duplex	Full-duplex	Dedicated channel

Table 1.1: Specifications and features of current interface standards for machine vision cameras [28, 29].

### Comparison between Camera Interfaces

In Table 1.1, I compare current interface standards for machine vision. Camera Link is the only interface that offers transmission not based on packets, meaning there are no duty cycles adding to the latency. Unlike Camera Link, other interfaces have a large communication overhead, mainly for two reasons. First, they support advanced features like networking and daisy-chains or error correction and image retransmission, so more complicated communication protocols are necessary. Second, the image data downlink is shared with the camera control uplink (full-duplex). This means bandwidth is not guaranteed and can be work-load dependent. Latencies are generally higher, since the shared communication bus can be busy. Camera Link features a dedicated camera control channel, whereby no camera drivers are required. Due to the simplicity of the Camera Link protocol, FPGA-based frame grabbers are inexpensive and transparent. Of all the available interface solutions, Camera Link is the only option for low-latency image processing.

## 1.4 State Analysis

The state of the ions can be inferred from the signal coming from the detector. For cameras, this signal is an image, which needs to be processed. The state discrimination algorithm used in our device is based on digital binning and thresholding. More complex algorithms exist [13], but are not considered for an FPGA implementation in this project. Since CMOS sensors have limited binning capabilities, they are only feasible in a special case of our algorithm. I compare different hardware for image processing and conclude that an FPGA is most suitable for low-latency image processing. Other projects [13] are based on slow post-processing of images on computers and are not suitable for fast feedback loops. I define the state analysis time  $t_{\text{analysis}}$  as the time after the full image is available to the state analysis hardware until the state of the ions is determined. Our specific implementation of the state analysis on our FPGA only has a few clock cycles state analysis time, see Chapter 2.

### 1.4.1 State Discrimination Algorithm

In this subsection, I describe the state discrimination algorithm which is implemented in Chapter 2. Its goal is to determine the state of an ion chain based on an input image. The algorithm consists of two phases: calibration and experiment. During calibration, pixels in a Region of Interest (ROI) that optimize the readout fidelity are selected for each ion. During the experiment, the state of each ion is determined by thresholding counts obtained from the pixels inside the ROI. Simulations of the algorithm in Section 4.1 are used to evaluate its performance and optimize the ROI and thresholds. In combination with higher magnifications, the algorithm can be used to mitigate optical cross talk in linear ion chains.

In the following, I compare and refer to Sections in [13]. Our protocol for state discrimination corresponds to the “Threshold Method” in Section 5.2.2. The time resolution gained with multiple exposures can be used in algorithms, see Section 5.2.3. However, reading out multiple frames is not feasible for low-latency applications, since the camera readout time is a limiting factor. In this project, I therefore only consider single exposures. Further, the spatial resolution of a camera can be used for a spatial maximum likelihood method, see Section 5.2.4. For a first proof of principle, this option is not considered for now, since implementing it on the FPGA would be more complex.

During calibration, a sequence of images is taken. From this, the mean photon numbers  $\lambda_{k,D}^{ij}$  and  $\lambda_{k,B}^{ij}$  for each pixel in case of ion  $k$  bright or dark

are extracted. I use this information to quantify the contribution of pixel ( $ij$ ) to the readout fidelity of ion  $k$  with the “signal to noise” ratio  $\overline{SNR}$ <sup>8</sup>:

$$\overline{SNR}_k^{ij} = \frac{\lambda_{k,B}^{ij} - \lambda_{k,D}^{ij}}{\lambda_{k,D}^{ij}}. \quad (1.16)$$

The  $N_{\text{ROI}}$  pixels with the highest  $\overline{SNR}$  are selected for each ion. This forms a Region Of Interest (ROI) around each ion in the image.

During the experiment, the bright and dark state of each ion is distinguished according to a threshold, see Section 3.1. Digital binning allows to alter the bright and dark state distributions before the threshold is applied. In digital binning, values from multiple pixels are summed digitally. In the algorithm, the sum of pixels inside the pre-calibrated ROI is compared to a threshold for each ion to determine its state.

To simulate digital binning, I consider the following: The total probability density function of a sum of random variables is given by the convolution of their individual probability density functions [23]. Following the linearity of expectation values and the Bienaymé formula for uncorrelated random variables, the binned ROI count distribution for an EMCCD can be approximated with the PGN model  $P^{\text{PGN}}(n|\lambda_{k,B/D})$  (1.10) with summed mean

$$\lambda_{k,B/D}G + \mu' := \sum_{i,j} (\lambda_{k,B/D}^{ij}G + \mu^{ij}) \quad (1.17)$$

and variance

$$2G^2\lambda_{k,B/D} + \sigma'^2 := \sum_{i,j} (2G^2\lambda_{k,B/D}^{ij} + \sigma^2). \quad (1.18)$$

I briefly discuss the binning capabilities of EMCCD and CMOS. The binned ROI has a higher total readout noise  $\sigma'$ , since the readout noise of each pixel is added. Due to the fact that EMCCDs are not readout noise limited, the summed readout noise is still negligible. For CMOS sensors however, digital binning is not feasible, since they are readout noise limited. CMOS therefore have restricted capabilities for image processing and can only compete when single ROI are considered. For EMCCDs, the limiting factor for digital binning is the internal noise source (CIC), which is a per

---

<sup>8</sup>To differentiate this ratio from the SNR quoted by camera manufacturer, it has an overline. The SNR is used to describe the ratio between signal incident on a pixel and the noise property of the camera. In contrast, the  $\overline{SNR}$  states the ratio between two signals - the ion and background. The background contains scattered laser light, optical cross talk and CIC, but does not contain further sensor properties.

pixel effect. Each pixel contributes to the mean of the binned dark state distribution with  $\lambda_{CIC}$ . This effect scales linearly with the number of pixels in the ROI  $N$  and reduces the readout fidelity for high  $N$ .

### 1.4.2 Hardware for Image Processing

The state discrimination algorithm described in subsection 1.4.1 is based on image processing. Here I compare three different hardware approaches to perform this task: Central Processing Units (CPU), Graphics Processing Units (GPU) and Field-Programmable Gate Arrays (FPGA). To integrate cameras into real time feedback loops, we require fast processing for low-latency ion readout. I conclude that FPGAs are the superior option with the lowest possible latency.

Image processing benefits from massive parallelization due to the 2D nature of the image. A serial processor like the **CPU** as used in [13] needs to process one pixel after another by running two loops over the image. The serial architecture is inherently slower and thus not suitable for low-latency image processing.

**GPU**-based systems<sup>9</sup> are widely used in the machine vision industry. Their parallel architecture allows them to process all pixels of a stored image at once. However, the image processing is based on software implementation and has a load-dependent overhead that can increase latency.

**FPGAs** contain arrays of programmable logic blocks that have user-customizable connections. This allows to implement image processing on the hardware level with deterministic execution times independent of load. Unlike GPUs, the parallelization for image processing comes from the fact that pixels can be processed on the fly as they arrive. This enables minimal state analysis times  $t_{\text{analysis}}$  of only few clock cycles which is ideal for our application, see subsection 2.3.1.

---

<sup>9</sup>e.g. <https://www.nvidia.com/en-us/autonomous-machines/embedded-systems-dev-kits-modules/>

## Chapter 2

# Implementation of Readout Device

In this Chapter, I explain how our readout device consisting of camera and FPGA acts as a standalone and can be integrated into existing control systems. I describe the technical details of the FPGA implementation performing the state analysis introduced in Section 1.4. It enables the use of cameras for real time feedback loops by performing fast image processing and state discrimination.

We use a commercial Abaco frame grabber board with a VC707 FPGA evaluation board to process frames transmitted over Camera Link, see subsection 1.3.3. The FPGA applies digital binning and thresholding to determine the ion states and uses a simple communication protocol to report the evaluated ion states to the control system. In contrast, the “Sinara Grabber” used with ARTIQ [30, 31] leaves image processing to the control system. Other systems [13] trigger the camera internally and use the camera as a reference to synchronize the experiment. We trigger the camera externally, which is more suited for time sensitive experiments. I conclude that our approach is more versatile and allows for easier integration into control systems.

To explain the features of the FPGA design, I give an overview of the logic cores implemented on the VC707. In particular, the hardware architecture of the state discrimination algorithm is designed to discriminate states of ten ions in parallel with negligible state analysis time. Since the ROI is stored using coordinates, the implementation supports arbitrary ROI shapes and both 1D and 2D arrays of ions. The resource usage of our FPGA design can be used to argue the scalability to systems with many ions. I conclude that

our implementation and hardware can be scaled to parallel readout of up to 400 ions. Apart from the state analysis, the FPGA can also measure camera readout time, control camera settings and transfer frames to a computer.

## 2.1 Integration into Control Systems

To enable real time feedback on trapped ions required by most QEC codes [2, 3], our readout device needs to be integrated into existing experiment control systems. In order to keep it adaptable to many different systems, it was designed as a standalone device. As an example, Fig. 2.1 shows our EMCCD-based readout device acting as a slave integrated into the “M-ACTION” [16] control system, which is represented as the master.

The design as a standalone readout device means a communication channel to the control system is required for transmitting the readout result. This introduces a state transfer time between slave (transmitter) and master (receiver) in Fig. 2.1. The connection is realized by two Low Voltage Differential Signaling (LVDS) pairs, one for the clock and one for the data. A simple serial communication protocol is implemented to transfer the ion states. It consists of a start bit, the state of the ions as a bit string (0 = dark, 1 = bright), a parity check bit and a stop bit, see Fig. 2.2 for an example. The parity check bit allows single error detection on the receiver. The serialization of the data introduces a state transfer time  $t_{\text{transfer}}$  given by

$$t_{\text{transfer}} = \frac{N_{\text{ion}} + 3}{f_{\text{CL}}}, \quad (2.1)$$

where  $N_{\text{ion}}$  is the number of ion states to be transmitted and  $f_{\text{CL}}$  the Camera Link clock frequency. The three additional cycles come from the start, stop and parity bit. Unlike a parallel connection, which would need one line per ion, a fast serial solution is scalable for systems with many ions.

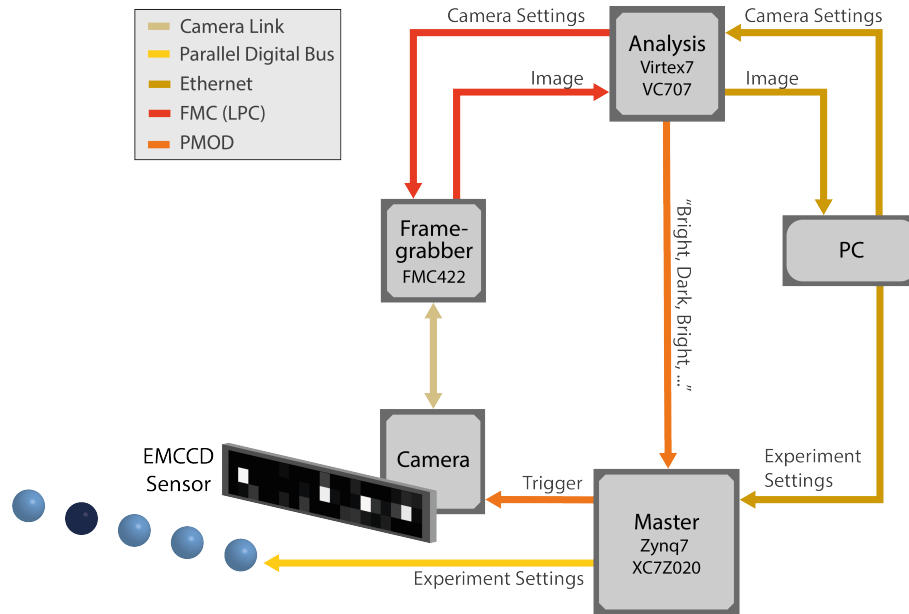


Figure 2.1: Integration of an EMCCD camera, frame grabber and state analysis FPGA into the ‘M-ACTION’ control system (master). Frame grabber and state analysis FPGA form a standalone device acting as a slave. Both master and slave can be initialized and externally monitored by a PC using Ethernet. After an initial calibration, the slave is ready for state analysis and requires no further user interaction. The master handles experimental sequences and feedback loops by controlling laser and trap parameters. It has the ability to request a readout of the ion chain by externally trigger the camera. The camera captures an image, and transmits the pixels to a frame grabber via Camera Link. The frame grabber is connected to the state analysis FPGA with FMC. The slave starts processing pixels as they arrive and implements the state discrimination protocol. The state of the ions is determined once the whole image is analyzed, upon which the state of the ions is passed along to the master.

## 2.2 Frame Grabber and FPGA Selection

Camera Link and FPGAs are essential tools for low-latency image processing used for ion state discrimination based on images, see Chapter 1. In the following, I motivate the choice of Camera Link frame grabber and FPGA board for this project.

We decide on an adapter board that converts Camera Link to the FPGA Mezzanine Card (FMC) standard<sup>1</sup>. It can be used with many FPGAs and allows for full control over the image processing. In contrast, different manufacturers offer commercial FPGA-based boards with built-in Camera Link interface<sup>2</sup>. Integrated commercial solutions have the drawback that they are restricted to certain FPGA hardware with potentially limited input and output (I/O) connections and might have limits in user programmability. We use the Camera Link frame grabber “FMC422” by Abaco<sup>3</sup>. Abaco provides an “FPGA board support package”, which contains verified firmware that runs on the Programmable Logic (PL) of the carrier FPGA. In particular, it was verified for the Xilinx VC707 evaluation board<sup>4</sup>. We decide on the VC707 board in combination with the FMC422 frame grabber, since this allows us to skip many time-consuming debugging steps involving Camera Link. A single FMC422 board has two Camera Link connectors and can support either a single Full/Medium or dual Base cameras. It is also able to supply power to the camera over the Camera Link cable.

The frame grabber and FPGA are put inside a custom 19" server enclosure shown in Fig. 2.3. The enclosure is designed to be used with up to two independent experiments performing parallel ion readout on different traps. Either two Base configuration cameras with a single FMC422 board or two Medium/Full cameras with two boards can be connected. It features the necessary communication outputs (Data and Clock) for transmitting the ion states to two master control systems, as well as four General Purpose Input and Outputs (GPIO).

---

<sup>1</sup>[https://www.xilinx.com/support/documentation/white\\_papers/wp315.pdf](https://www.xilinx.com/support/documentation/white_papers/wp315.pdf)

<sup>2</sup>e.g. <http://www.ni.com/pdf/product-flyers/ni-frame-grabbers.pdf>

<sup>3</sup><https://www.abaco.com/download/fmc422-user-manual>

<sup>4</sup>The VC707 hosts a Virtex-7 based FPGA chip and two FMC connectors, see [https://www.xilinx.com/support/documentation/boards\\_and\\_kits/vc707/ug885\\_VC707\\_Eval\\_Bd.pdf](https://www.xilinx.com/support/documentation/boards_and_kits/vc707/ug885_VC707_Eval_Bd.pdf)

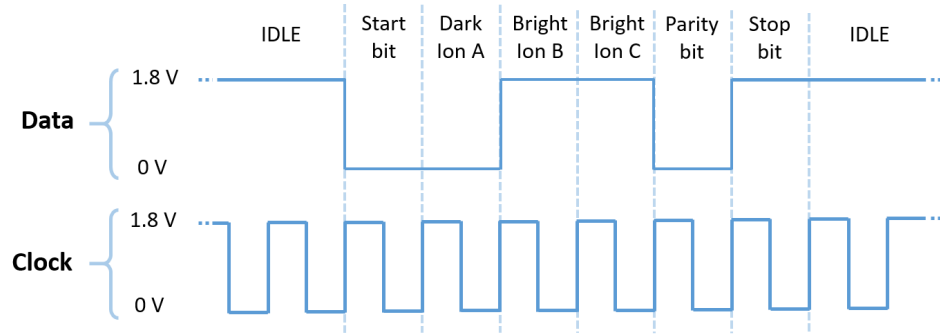


Figure 2.2: Example timing diagram of the communication protocol used for the transmission of ion states between slave and master. Shown are data and clock signals sent by the transmitter for three ions in state dark-bright-bright. The parity bit in this case is 0 ( $0 + 1 + 1 = \text{even}$ ). The start bit is 0 and the stop bit is 1.



Figure 2.3: Preliminary layout of the enclosure containing the FPGA and frame grabber board. Shown is the front view without the top lid. The front panel features 12 SMA connectors, one FMC422 board, a user controllable LCD screen and a power button. Inside it hosts the VC707 evaluation board, a power supply (240 V to 12 V, 100 W Max.) and a relay. On the back, there are power, USB and Ethernet feedthroughs. Fans on the side and back provide airflow for cooling.

## 2.3 FPGA Design and Hardware Architecture

In this section, I discuss the design implemented on the Virtex-7 FPGA on the VC707 evaluation board. Custom logic cores handle tasks such as fast state analysis of ions and measurements of camera readout time. The hardware architecture of the state analysis enables massive parallelization of image processing, which makes processing times negligible. The latency measurement is used in Section 4.2 to validate the readout time of a FT EMCCD camera. The FPGA design was verified with behavioral simulations using Vivado Simulator. The real time verification was performed using an *Andor iXon 888* camera.

Figure 2.4 shows a simplified overview of the FPGA hardware architecture. The individual logic cores are explained in Subsection 2.3.1. The firmware is stored on a BPI Flash Memory on the VC707 and automatically configured on every startup.

### 2.3.1 Logic Cores

In the following, I explain the most relevant FPGA logic cores from Fig. 2.4. They are responsible for tasks such as frame grabbing, image analysis, camera control, latency measurement or communication with control systems.

The **AXI-TCPIP engine** translates Ethernet commands coming from a PC into AXI4-Lite<sup>5</sup> compliant read and write access. It is responsible for the AXI bus that connects and controls all the logic cores. The **CL Fgrabber** core handles the Camera Link protocol and deserializes the data coming from the camera. User accessible registers (AXI-regs) are used to configure the frame grabber. The CL Fgrabber core also features the ability to generate test images and an internal Camera Link clock without a camera attached. The pixel data, frame and line valid signals, as well as Camera Link clock and frame grabber status are intercepted in the Abaco code and revealed to the user logic. The **CL UART** core manages the serial communication with the camera over Camera Link. The commands, which are specific to a camera, are written to and read from user accessible registers. They are used to configure camera settings and retrieve camera information. The **WMF Capture** core is used to store images into Block RAM (BRAM). The frames in the BRAM can be transmitted over Ethernet to a PC using an AXI4-Streaming interface. Storing frames is not required for the operation of the state discrimination protocol, but can be useful for debugging. The **Latency**

---

<sup>5</sup>[https://www.xilinx.com/support/documentation/ip\\_documentation/ug761\\_axi\\_reference\\_guide.pdf](https://www.xilinx.com/support/documentation/ip_documentation/ug761_axi_reference_guide.pdf)

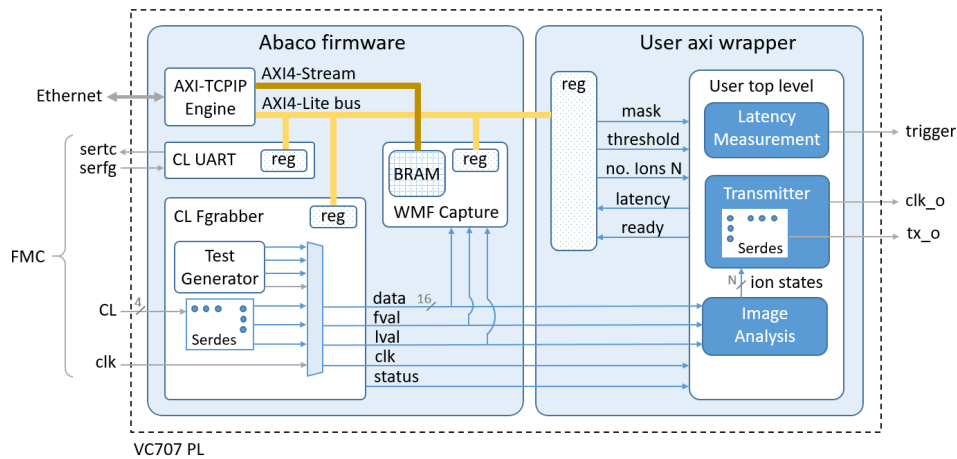


Figure 2.4: Simplified FPGA design of firmware running on the VC707 PL. Alongside the Abaco firmware, there are three user cores running on the PL. They are contained within the “User AXI wrapper”, which offers user accessible registers. These registers are connected to the Abaco AXI4-Lite bus, which can be controlled via Ethernet. A Camera Link Base camera is attached via the frame grabber board to the FMC connection. The camera is controlled via “serfc” and “serfg” and provides the Camera Link clock “clk”. Inside the Abaco firmware, the pixel values as well as the fval and lval signals are intercepted and routed to the Image Analysis core, where the image is processed and the ion states are determined. The master control system is connected to “clk\_o” and “tx\_o”, which implement the communication protocol from Section 2.1. “trigger” is only used to measure camera readout times and connected to the external trigger input of the camera.

**Measurement** core is used to measure the camera readout time. It sends a signal to the external trigger of a camera and runs a counter until the first pixel arrives in the frame grabber. Another counter starts and runs until the last pixels arrives. The sum of these two counters is the camera readout time plus exposure time. The **Transmitter** core implements the communication protocol from Section 2.1. It transmits the readout result as the state of  $N_{\text{ion}}$  ions to the master control system. The **Image Analysis** core implements the state discrimination algorithm from Section 1.4.1. Figure 2.5 shows the hardware architecture of this logic core. In order to meet FPGA timing requirements, I store the signals for the “Mask matched” and the reduction OR thereof in registers. This delays the signals by two clock cycles, resulting in an effective state analysis time given by

$$t_{\text{analysis}} = \frac{2}{f_{\text{CL}}}, \quad (2.2)$$

where  $f_{\text{CL}}$  is the Camera Link clock frequency.

All of the logic cores above are controlled by a Python script. It builds on “UnitAPI”<sup>6</sup>, a precompiled C++ library provided by Abaco, which interacts with the AXI-TCPIP engine. Only the low-level UnitAPI functions are required for operation and have been wrapped in Python functions. They feature opening and closing Ethernet connections, address-based reading from and writing to AXI registers for configuration and receiving data for image acquisition. I represent each logic core as a Python class. The classes store register addresses and handle initialization procedures. I also implement functions for tasks such as capturing frames, calibrating ROI coordinates and measuring camera readout time.

### 2.3.2 Clocking

The FPGA design contains two clock domains. The camera (or alternatively the internal test clock) provides the Camera Link clock with frequency  $f_{\text{CL}} = 20 - 80$  MHz, depending on the camera. This clock is used with all logic cores described in Subsection 2.3.2, except for the AXI bus. The AXI-TCPIP engine and AXI controlled registers run at  $f_{\text{AXI}} = 125$  MHz.

In a later implementation, the state transfer time in Eq.(2.2) could be decreased by introducing an additional clock domain for the transmitter. It could make use of the VC707’s Output Parallel-to-Serial modules

---

<sup>6</sup><https://www.abaco.com/download/unitapi-user-manual>

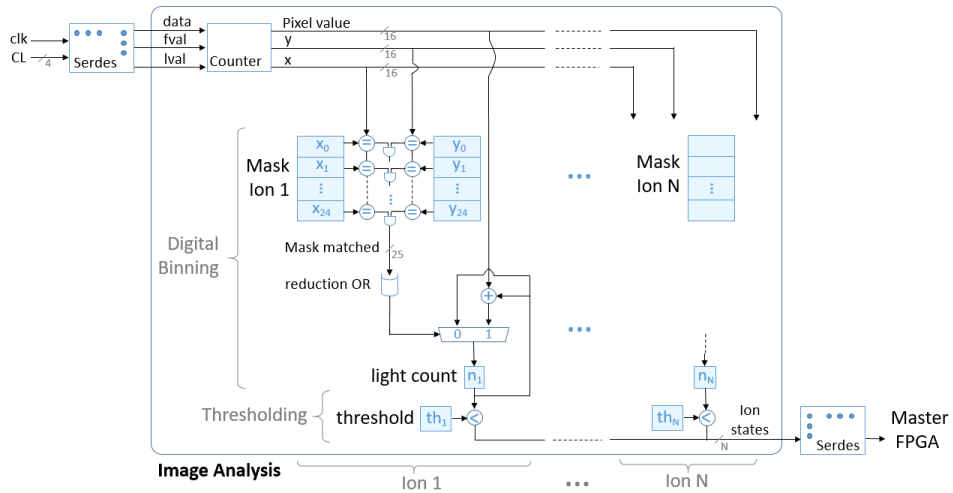


Figure 2.5: Detailed Hardware Architecture of the Image Analysis core. The signal from Camera Link is deserialized by the frame grabber before it reaches the Image Analysis core. The frame and line valid signals are converted to coordinates  $x$  and  $y$  with the help of a counter. Each ion has its pre-calibrated ROI pixels stored as a list of mask coordinates in the user registers. The image analysis is done on the fly and in parallel: As soon as a pixel arrives, its coordinates are compared with all mask coordinates simultaneously. If there is a match, the pixel value gets added to the corresponding ion count. This implements digital binning of the pixels inside the ROI of a particular ion. At the end of the frame, each ion count gets compared to its threshold and the state of the ion is determined. The final result is passed along to the transmitter as a bit string of the  $N$  ion states, where it gets serialized and sent to the master control system.

(OSERDES) with double data rate at a theoretical maximum of 800 MHz I/O Clock Network frequency (BUFIO)<sup>7</sup>.

### 2.3.3 FPGA Simulation

I use Vivado Simulator to verify the FPGA design. The simulation is based on a test bench provided by Abaco, which deploys a behavioral model to simulate the AXI-TCPIP engine. It emulates the communication between PC and FPGA by reading Ethernet commands from a script and executing the corresponding AXI read or write access. It can also use a model of the Camera Link protocol that imports images and outputs the corresponding (Base) Camera Link signals.

## 2.4 FPGA Hardware Resource Usage

In this section, I discuss the hardware resource usage of our FPGA design. The main contributions come from the frame buffer, calibration and image analysis process. As an example, pixels with 16 bits are used, as this is the typical pixel depth provided by EMCCD cameras considered for this project. We do not restrict ourselves to specific frames sizes, since future applications may make use of a variety of cameras. I conclude that the current design and hardware can be scaled to 400 ions, limited by the amount of slice LUTs used in the state discrimination protocol. Potential improvements to the implementation could optimize the resource usage in the future.

Figure 2.6 shows the hardware resource usage for the finalized design. The contributions are discussed below.

### 2.4.1 Frame Buffer

The frame grabber can buffer images in the “WMF capture” core using Block RAM (BRAM). The VC707 features 1030 tiles with 36 Kb BRAM each<sup>8</sup>. The BRAM usage can be calculated with

$$\text{Number of BRAM used} = \frac{\text{Number of pixels} \times \text{Pixel depth}}{\text{BRAM size}}. \quad (2.3)$$

---

<sup>7</sup>[https://www.xilinx.com/support/documentation/application\\_notes/xapp585-lvds-source-synch-serdes-clock-multiplication.pdf](https://www.xilinx.com/support/documentation/application_notes/xapp585-lvds-source-synch-serdes-clock-multiplication.pdf)

<sup>8</sup>[https://www.xilinx.com/support/documentation/user\\_guides/ug473\\_7Series\\_Memory\\_Resources.pdf](https://www.xilinx.com/support/documentation/user_guides/ug473_7Series_Memory_Resources.pdf)

Name	Slice LUTs (303600)	Slice Registers (607200)	F7 Muxes (151800)	F8 Muxes (75900)	Slice (75900)	LUT as Logic (303600)	LUT as Memory (130800)	LUT Flip Flop Pairs (303600)	Block RAM Tile (1030)
vc707_fmc422_axi	19567	21807	1689	796	8844	19364	203	5758	474
axi_csd_ax_0 (axi_csd_ax)	118	99	19	0	38	118	0	56	0
axi_cmd8_mux_0 (axi_cmd8_mux)	114	0	0	0	68	114	0	0	0
axi_fmc422_0 (axi_fmc422)	2785	2614	65	32	1143	2651	134	1415	0
axi_j2c_master_0 (axi_j2c_master)	665	876	5	0	276	665	0	396	0
axi_intrc16_0 (axi_intrc16)	482	754	0	0	211	482	0	338	1
axi_texp_engine_vc707_0 (axi_texp_engine_vc707)	5722	5895	7	0	2327	5653	69	2362	13
axi_wfm_capture_0 (axi_wfm_capture)	2165	2011	504	252	1250	2165	0	670	456
axi_wb256towh64_0 (axi_wb256towh64)	110	184	0	0	68	110	0	72	4
user_if_inst (user_if)	7409	9374	1089	512	3724	7409	0	430	0
axi_lite_mux_inst0 (cmd00_mux_wrapper)	64	147	0	0	56	64	0	29	0
user_axi_wrapper_inst (AXI_Reg_gen_v1_0)	7346	9227	1089	512	3688	7346	0	401	0
AXI_Reg_gen_v1_0_S00_AXI_inst (AXI_Reg_gen_v1_0_S00_AXI)	7346	9227	1089	512	3688	7346	0	401	0
user_top_inst (user_top)	3792	499	1	0	1777	3792	0	356	0
latency_measurement_inst (latency_measurement)	81	179	0	0	61	81	0	51	0
thresholding_inst (thresholding)	3642	298	0	0	1706	3642	0	287	0
Transmitter_inst (Transmitter)	67	20	1	0	20	67	0	18	0

Figure 2.6: FPGA resource utilization on the VC707 by functional block. The Abaco IP cores are marked orange, the user logic are marked blue. This particular implementation can perform parallel readout of 10 ions with maximum ROI size of 25 pixels per ion. It performs the state discrimination protocol described in Subsection 1.4.1. 456 BRAM is used for frame buffering. 8320 Slice registers are used to store ROI coordinates and thresholds for each ion. 7200 Slice LUTs are used for state discrimination.

Using all available BRAM, the VC707 can buffer a total of 2.3 Million pixels, which is approximately one frame of size  $1500 \times 1500^9$ . A future implementation could use DDR3 memory (1 GB) featured on the VC707 to store up to 500 million pixels. EMCCDs considered in this project typically have small frame sizes to achieve fast readout times (e.g.  $128 \times 128$ ), see Section 4.2. The VC707 hardware is future proof, since it is also capable of handling larger frame sizes.

## 2.4.2 Calibration

The state analysis requires the calibration of a ROI and threshold for each ion, see Subsection 1.4.1. I store the ROI pixels in slice registers as two 16 bit values for the x and y coordinates. The 32-bit threshold for each ion is also saved in a slice register. Per ion, a total of 26 registers (32-bit) are used. The current implementation allows for 10 ions with a ROI size of 25 pixels each, which needs  $10 \times (26 \times 32) = 8320$  registers, see Fig 2.6.

Using all available slice registers on the VC707, it is possible to calibrate the device for a total of 717 ions. This is not the factor that limits scalability to many ions. Still, an improved implementation could use BRAM to store the calibration data, where single BRAM tile would be able to store the configuration of 44 ions.

<sup>9</sup>The current implementation only uses half of the available resource (456 BRAM).

### 2.4.3 Image Analysis

The “Image Analysis” core requires Look up tables (LUTs) to perform the state discrimination. The relation between used slice LUTs and number of operations in the algorithm is non-trivial. As an estimate, I use the number of used LUTs from the current implementation for 10 ions and scale it to many ions. For 720 slice LUTs per ion, a total of 400 ions can be processed in parallel using all the available LUTs on the VC707. This is the limiting factor for the scalability of the design to many ions<sup>10</sup>.

## 2.5 Comparison to ARTIQ Sinara Grabber

In an effort towards using cameras for low-latency parallel ion readout, a direct integration of a Camera Link frame grabber into the core FPGA of the ARTIQ system has been in development [31]. The “Sinara Grabber” hardware and firmware is still undergoing testing at the time of writing. I compare this approach to ours and conclude that there are some considerable differences that make our readout device superior.

The Sinara Grabber board is similar to our frame grabber, but doesn’t use a standard connector like FMC. The Sinara readout device is not designed as a standalone. Instead of using an external FPGA that handles the image analysis and only transfers the final state of the ions, the Sinara Grabber passes along the raw Camera Link stream to the master FPGA. De-serialization, digital binning and state identification are performed on the master FPGA. This approach requires more I/O and hardware resources on the master FPGA, making an integration into a different control system less feasible. The Sinara Grabber only supports a limited range of cameras. It relies on an extra connection apart from Camera Link (e.g. USB or Ethernet) for two reasons: First, it does not implement the serial communication between the FPGA and camera, so there is no way to control the camera over Camera Link. Second, there is no frame buffer implemented on the FPGA. Any images required for calibration need to be captured on a PC using the camera control software. In particular, the *Nuvu HNU 128* camera selected for this project does not work with the Sinara Grabber. Further, the Sinara FPGA implementation of state analysis only supports rectangular ROI around the ions. In contrast, our device supports arbitrary ROI shapes

---

<sup>10</sup>Xilinx Ultrascale+ FPGAs provide more hardware resources than Virtex-7 and can potentially be used if more than 400 ions are targeted, see <https://www.xilinx.com/products/boards-and-kits/vcu118.html>

for ions in arbitrary lattices, can interface all cameras compatible with Camera Link and has minimal work load on the master system. This makes our approach more versatile and applicable to different control systems.

## Chapter 3

# Criteria for Readout Devices

Both the fidelity and duration of readout limit the fidelity of quantum algorithms that rely on measurement-based feedback, in particular QEC codes [2, 3, 10]. This motivates the design of a readout device with the goal of low-latency and high-fidelity ion readout. In this chapter, I introduce the readout fidelity and state discrimination time as our two design criteria. The readout fidelity describes how well the qubit states can be distinguished in an experiment. The state discrimination time gives the duration required to perform the single-shot ion readout. The readout parameters introduced in previous chapters influence the two design criteria, with the exposure time taking a special role since it influences both. The two criteria are calculated and used to quantify the performance of readout devices in Chapter 4.

Unlike others, e.g. Section 5.1.2 in [13], I avoid comparing different detectors using the Signal-to-Noise ratio (SNR). I find that the SNR is not a good measure for the quality of readout devices based on EMCCD sensors. Using the readout fidelity instead allows me to quantify how different technologies perform in Section 4.3.

### 3.1 Readout Fidelity

I now define how the quality of readout can be characterized by the readout fidelity  $\mathcal{F}$  or equivalently by the readout infidelity (readout error)  $\epsilon = 1 - \mathcal{F}$ . It gives a measure to what precision the state of qubits can be determined and is calculated in Section 4.1 for our readout device.

In an experiment, the readout fidelity can be evaluated by repeatedly preparing the ion in a known state and performing readout. The readout

infidelity is given by the average [11]

$$\epsilon = \frac{1}{2}(\epsilon_B + \epsilon_D) , \quad (3.1)$$

where  $\epsilon_B$  is the fraction of trials where the ion was prepared in bright state but was incorrectly identified as dark and vice versa for  $\epsilon_D$ . This definition is independent of the state discrimination protocol.

For a state discrimination based on thresholding, the theoretical readout fidelity can be characterized by the detector count distributions from Section 1.3. I define the bright (or dark) state distribution of ion  $k$  as the normalized probability density function  $P(n|\lambda_{k,B/D})$  of detector counts when the ion was prepared in the bright (or dark) state. As an example, Fig. 3.1 shows typical bright and dark state distributions for an EMCCD camera. The distribution corresponds to the probability that  $n$  counts are measured for a bright (or dark) ion. The main difference between a dark and bright ion is the mean photon number incident on the detector  $\lambda_{k,B/D}$ . The exact shape of the distribution depends on the type of detector, see Section 4.3.

In a thresholding algorithm, a count threshold  $t_n^k$  is used to decide whether ion  $k$  is bright or dark. For all counts  $n \leq t_n^k$  the ion is considered dark, where as for counts  $n > t_n^k$  it is considered bright. Due to shot and detector noise, the bright and dark state distributions have tails that overlap and go beyond the threshold. “Dark counts” below the threshold have a high probability to belong to a dark ion, but there is a finite probability that they belong to a bright ion. This can result in an incorrect readout and represents  $\epsilon_B$ , vice versa for  $\epsilon_D$ . Equivalent to Eq. 3.1, the readout infidelity is given by the average between the two areas underneath the distributions that belong to the “wrong” state

$$\epsilon = \frac{1}{2} \left( \int_0^{t_n^k} P(n|\lambda_{k,B})dn + \int_{t_n^k}^{\infty} P(n|\lambda_{k,D})dn \right) . \quad (3.2)$$

These areas depend on the threshold and are minimized when the threshold is at the intersection between the two distributions. In this case, the readout error is proportional to the overlap area

$$\epsilon = \frac{1}{2} \left( \int_0^{\infty} \min(P(n|\lambda_{k,B}), P(n|\lambda_{k,D}))dn \right) . \quad (3.3)$$

The average and variance of counts of the two distributions introduced above is proportional to the corresponding mean photon number, see Subsection 1.3.1 in case of the EMCCD. A higher mean photon number shifts

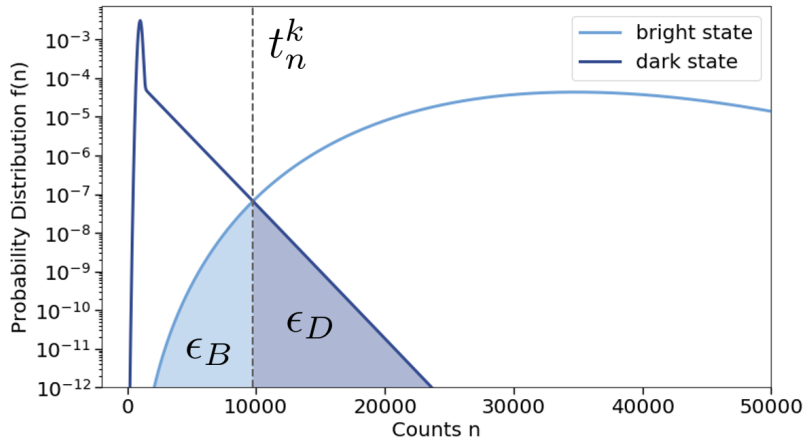


Figure 3.1: Typical EMCCD count distribution for an ion prepared in bright or dark state. This example shows scenario 1 with ROI 1 from Chapter 4. The mean photon number in this case is  $\lambda_{k,B} = 29.621$  or  $\lambda_{k,D} = 0.092$ . I choose the optimal threshold  $t_n^k = 9763$  at the intersection between the two distributions (dotted line). The area underneath the bright distribution for counts below the threshold represent the fraction of “wrong” counts for an ion prepared in bright state  $\epsilon_B$ , vice versa for  $\epsilon_D$ . The readout infidelity is the average of the two areas and yields  $\epsilon = 7.94 \times 10^{-5}$  from numerical calculations.

the count distribution to higher counts on the right but also broadens the distribution due to shot noise. Since the standard deviation scales with the square root of the average, the shifting is larger than the broadening of the distribution. Thus, a smaller overlap between the bright and dark state distribution can be achieved with a larger difference in dark and bright photon number, making state discrimination with high fidelities possible.

I now explain how the mean photon number can be calculated for a bright and dark ion. In our algorithm, the mean photon numbers are acquired by digital binning ( $\sum_{i,j}$ ) of multiple pixels, see Subsection 1.4.1. The mean photon number incident on pixel  $(ij)$  for ion  $k$  in **bright state**  $\lambda_{k,B}^{ij}$  is given by the signal of ion  $k$  and the background:

$$\lambda_{k,B}^{ij} = \lambda_{k,D}^{ij} + w_k^{ij} R_B t_{\text{exp}} \eta Q , \quad (3.4)$$

where  $w_k^{ij}$  is the weight from ion  $k$  on pixel  $(ij)$  from Eq. 1.6,  $R_B$  the ion fluorescence rate,  $t_{\text{exp}}$  the exposure time,  $\eta$  the collection efficiency of the imaging setup and  $Q$  the detector quantum efficiency.

The mean photon number incident on pixel  $(ij)$  for ion  $k$  in **dark state**  $\lambda_{k,D}^{ij}$  is given by the background only, consisting of scattered laser light, internal noise and optical cross talk from all other ions:

$$\lambda_{k,D}^{ij} = u^{ij} R_L t_{\text{exp}} \eta Q + \lambda_{\text{CIC}} + \sum_{l \neq k} \sigma_l w_l^{ij} R_B t_{\text{exp}} \eta Q , \quad (3.5)$$

where  $u^{ij}$  is given by Eq. 1.8,  $R_L$  the rate of scattered laser light per area,  $\lambda_{\text{CIC}}$  the CIC noise, and the state of the neighboring ions  $\sigma_l$  given by

$$\sigma_l = \begin{cases} 0 & , \text{ ion } l \text{ in dark state} \\ 1 & , \text{ ion } l \text{ in bright state} \end{cases} . \quad (3.6)$$

Figure 3.2 summarizes this section and shows an overview of the experimental parameters influencing the readout infidelity.

Instead of the readout fidelity, the camera Signal-to-Noise Ratio (SNR)<sup>1</sup> is often quoted to compare detectors and predict the readout quality, e.g. [13]. The SNR formula considers the ion signal, background and the sensor noise properties. Even though it combines the most important experimental parameters, I find that it is not a good measure for the readout fidelity of EM-CCD sensors. The reason being that it doesn't incorporate the exact shapes of the bright and dark tails, which are also asymmetric, see Fig. 3.1. I could

<sup>1</sup>[https://camera.hamamatsu.com/jp/en/technical\\_guides/calculating\\_snr/index.html](https://camera.hamamatsu.com/jp/en/technical_guides/calculating_snr/index.html)

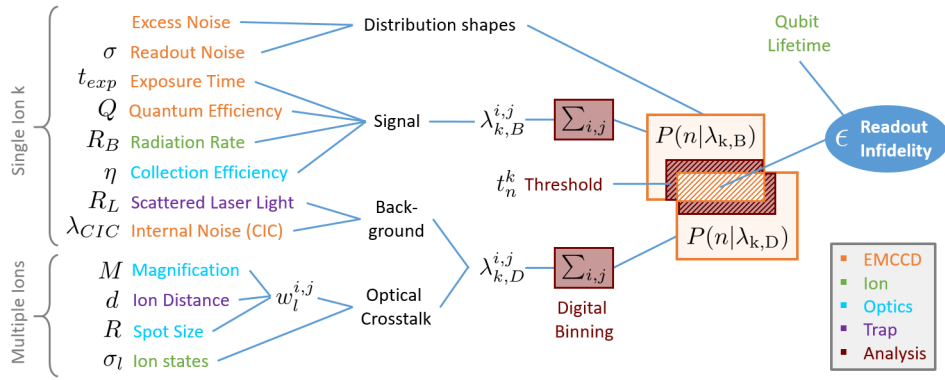


Figure 3.2: Dependencies of the readout infidelity  $\epsilon = 1 - \mathcal{F}$  on experimental parameters for single and multiple ion readout. The parameters are listed according to their most significant contribution to either distribution shape, ion signal, background or optical cross talk. The parameters are classified with color to either EMCCD, ion, optics, trap or analysis. The mean photon numbers are obtained from digital binning and influence the separation between bright and dark state distribution. The state of the ion is discriminated with a threshold. The overlap between dark and bright state distribution gives the readout infidelity.

only find a clear relation between the SNR and readout fidelity for perfectly symmetric distributions, but not for general distributions with asymmetric tails (which are inherent to the problem due to shot noise). I conclude that the SNR is not an absolute measure for the quality of state discrimination based on thresholding and not suitable to compare different sensor technologies for ion readout.

### 3.2 State Discrimination Time

Here I introduce the state discrimination time as a measure of readout duration. It is used in Chapter 4.2 to predict the readout duration for our readout device.

I define the state discrimination time  $t_{\text{disc}}$  as the difference in time between the request for an ion readout by the experiment control system and the arrival of readout results. It is given by the sum of latencies introduced by different processes involved in ion readout:

$$t_{\text{disc}} = t_{\text{exp}} + t_{\text{read}} + t_{\text{analysis}} + t_{\text{transfer}} , \quad (3.7)$$

where  $t_{\text{exp}}$  is the exposure time,  $t_{\text{read}}$  the camera readout time given by Eq. 1.11,  $t_{\text{analysis}}$  the state analysis time given by Eq. 2.2 and  $t_{\text{transfer}}$  the time required to transfer the ion states to the control system given by Eq. 2.1.

## Chapter 4

# Simulation of Readout Devices

In this chapter, I simulate the behavior of various devices for parallel readout of linear ion chains considering realistic experimental parameters. This allows me to compare different readout systems, optimize readout parameters and estimate the expected performance for low-latency and high-fidelity parallel readout of ions. In particular, I evaluate the two design criteria readout fidelity and state discrimination time defined in Chapter 3 for our readout device.

The experimental parameters used in the simulations are presented in Table 4.1. We select the *Nuvu HNU 128 AO* as our detector. The Nuvu is the only EMCCD on the market that fulfills all our criteria and is suitable for low-latency applications, since it features a low pixel count and a Camera Link interface. Further, I compare state-of-the-art EMCCD to CMOS and multi-channel PMT detectors for parallel ion readout and conclude that EMCCDs are the best option at the time of writing. The details of the detectors used in the comparison can be found in Table 4.2.

For the readout fidelity, parameters such as magnification, threshold and exposure time are used as variables and optimized for fixed ion type, ion-ion spacing and geometry. By doing so, we can achieve a readout infidelity below  $10^{-4}$  in our setup for low magnifications. I find that for our device, the main contributions to the state discrimination time are the exposure and camera readout time. Since it is limiting, we use measurements of the camera readout time to verify the model proposed in subsection 1.3.1. This is the first time that the camera readout time has been evaluated for the use of FT EMCCD cameras for low-latency ion readout. I conclude that, to reach readout infidelities of  $10^{-4}$  with our setup, we require a state discrimination time of 225  $\mu\text{s}$ . In comparison, Burrell [13] was able to achieve similar infi-

delities with EMCCD exposure times of 400  $\mu\text{s}$ , readout times of 5120  $\mu\text{s}$  and post-processing state analysis which is orders of magnitudes slower. Using multi-channel PMTS, infidelities of  $10^{-2}$  were achieved in 150  $\mu\text{s}$  [12].

## 4.1 Readout Fidelity

High-fidelity single-shot readout with infidelities on the order of  $10^{-4}$  is desired for fault tolerant quantum computation [8, 9]. In the following, I show that we expect to achieve such high readout fidelities in our readout device using an EMCCD camera and a state discrimination protocol based on digital binning and thresholding.

To reduce the parameter space, I only consider scenarios that are “scalable”. In these scenarios, all ion centers on the image plane are in the center of pixels. This guarantees that the same readout fidelity can be achieved for all ions in an arbitrary long ion chain. Scalable scenarios for chains with ion spacing  $d$  imaged onto a pixel of width  $P_x$  impose the following condition on the magnifications:

$$M_p = (p + 1) \times \frac{P_x}{d} \quad (4.1)$$

for  $p \in \mathbb{N}$ . For increasing magnifications, more pixels are put in between the ion centers. “Scenario  $p$ ” has  $p$  pixels in between the center of two neighboring ions. Two different scenarios for ion readout are discussed in detail. First, scenario 1 with a low magnification of  $M = 9.6$ , where the ion disk is mainly contained within one pixel. Second, scenario 16 with a high magnification of  $M = 81.6$ , where the ion disk is spread over multiple pixels. I conclude that for our setup, low magnifications tend to have a better readout fidelity, but low and high magnifications show different sensitivity to ion position shifts. Depending on what precisions are accessible in the experiment, a more robust magnification can be chosen. Optical cross talk is present for parallel readout of ions and imposes a state dependence on the readout fidelity and threshold. Since optical cross talk is short range, only nearest neighbors need to be considered and parallel readout is scalable for long ion chains [13]. Thus, three ions in a chain suffice to fully characterize the readout including cross talk in our simulations. The readout fidelity that is evaluated for the middle ion is therefore also applicable for ions in an arbitrary long ion chains. Unlike Eq. (5.12) in [13], we don’t consider the average readout fidelity over all possible ion states. Instead, we calculate the fidelity for the worst case where both neighboring ions are bright. I conclude that using a fixed threshold optimized for this case still results in a lower

Table 4.1: Experimental parameters of the detector, ion, optics and state analysis used in the simulations.

<b>Detector</b>	<i>Nuvu HNU 128 AO</i>
Exposure Time $t_{\text{exp}}$	120 $\mu\text{s}$
Conversion Factor $\beta$	4.16 $e^-$ per count
Offset $\mu$	1000
<b>Ion</b>	$^{40}\text{Ca}^+$
Number of Ions - State	3 - BBB
Ion - Ion Distance	5 $\mu\text{m}$
Fluorescence Wavelength	397 nm
Einstein Coefficient $A_{21}$	$132 \times 10^6 \text{ s}^{-1}$
Laser Intensity $I/I_{\text{sat}}$ <sup>a</sup>	1
Fluorescence Rate $R_B$	$2.64 \times 10^7 \text{ s}^{-1}$
Fluorescence Power $P_B = R_B \hbar \omega$	$1.32 \times 10^{-11} \text{ W s}^{-1}$
Rate of Scattered Laser $R_L$	$2.3 \times 10^{14} \text{ s}^{-1} \text{ m}^{-2}$
Scattered Laser Intensity $I_L/I_{\text{sat}}$	$4.42 \times 10^{-7}$
Qubit Lifetime	$\infty$
<b>Optics</b>	<i>Schwarzschild-type Objective</i> <sup>b</sup>
Numerical Aperture NA	0.55
Collection Efficiency $\eta$	2.33 %
Magnification M	9.6, 81.6
Spot Radius $R_{\text{Airy}}$	0.9259 $\mu\text{m}$ (at $M = 1$ )
equivalent NA	0.25
<b>State Analysis</b>	Digital Binning, Thresholding
No. of pixels in optimal ROI $N_{\text{ROI}}$	1, 21

<sup>a</sup> For the  $S \leftrightarrow P$  transition,  $I_{\text{sat}} = 933.82 \text{ W m}^{-2}$ .

<sup>b</sup> Details can be found in [17].

Table 4.2: Parameters of state-of-the-art EMCCD, CMOS and PMT detectors. The performance of the three detectors is compared in Section 4.3.

<b>Detector</b>	<i>Nuvu HNU 128 AO</i> <sup>a</sup>	<i>Hamamatsu H7260- 200</i> <sup>b</sup>	<i>Photometrics Prime 95B Blue</i> <sup>c</sup>
Sensor Type	EMCCD	Multi-channel PMT	CMOS
Quantum Efficiency at 397 nm (%)	45 (90) <sup>d</sup>	40	87
Readout Noise per pixel (e <sup>-</sup> )	< 0.1 ( $G = 5000$ )	-	2 (rms)
Internal Noise per pixel (e <sup>-</sup> )	0.005 (CIC)	-	-
Resolution (px $\times$ px)	128 $\times$ 128	1 $\times$ 32	1200 $\times$ 1200
Pixel Size ( $\mu\text{m} \times \mu\text{m}$ )	24 $\times$ 24	800 $\times$ 7000	11 $\times$ 11
Electronic Crosstalk (%)	-	3 (0.6) <sup>e</sup>	-
Gap between pixels (mm)	-	0.2	-
Frame Rate (fps) at ROI	1838 (64 $\times$ 64)	$\sim 10^8$ (1 $\times$ 32)	1500 (5 $\times$ 1200)
$\lambda_B$ for scenario 1 at ROI 1	34.56	15.54	33.40
$\lambda_D$ for scenario 1 at ROI 1	0.11	0.23	0.10
limited by	excess noise, CIC	shot noise, low Q	readout noise
Probability Density Function	PGN Eq. (1.10)	Continuous Poissonian	MPM Eq. (1.14)

<sup>a</sup> [http://www.nuvucameras.com/wp-content/uploads/2018/01/NUVUCAMERAS-HNu128\\_AO.pdf](http://www.nuvucameras.com/wp-content/uploads/2018/01/NUVUCAMERAS-HNu128_AO.pdf)

<sup>b</sup> [https://www.hamamatsu.com/resources/pdf/etd/LINEAR\\_PMT\\_TPMH1325E.pdf](https://www.hamamatsu.com/resources/pdf/etd/LINEAR_PMT_TPMH1325E.pdf). Used in [4, 12].

<sup>c</sup> <https://www.photometrics.com/products/datasheets/Prime95B-Datasheet.pdf>.

<sup>d</sup> Upcoming version (2019) with increased sensitivity in the UV region.

<sup>e</sup> For neighboring channels, the electronic cross talk is 3 %, for next-nearest neighbors 0.6 %.

infidelity for all other states. This allows us to claim that the calculated readout fidelity is a lower bound. With the EMCCD in our setup, upper-bound readout infidelities of  $10^{-4}$  can be achieved with  $120\ \mu\text{s}$  exposure time.

I will now give a brief introduction how the fidelity is calculated numerically and compare it to Burrells implementation in [13]. A Python software package allows the user to create and import configuration files that describe detectors, optics and ions. The parameters given in the files are used to create count distributions for each pixel. For the EMCCD, the PGN model from Section 1.3.1 is used. In contrast, Burrell uses the Tubbs model, see Section 5.1.3 in [13]. The two models describe the EMCCD equally well from a practical point of view [22], but the PGN model is easier to implement numerically. Digital binning is achieved by summing pixel parameters according to Eq. (1.17) and (1.18). The binned count distribution is discretized to integer values. From this, the readout fidelity is numerically evaluated from the discretized integral (3.2). Using this numerically fast implementation allows us to explore the parameter space efficiently. In contrast, Burrell generates millions of images for each set of parameters by sampling from the pixel count distributions and performs digital binning and thresholding on them. The readout fidelity is then obtained from the number of correct trials for ions prepared in bright or dark state like in an experiment using Eq. (3.1).

#### 4.1.1 Spatial Distribution and $\overline{SNR}$

In this subsection, I discuss how the state discrimination algorithm from Section 1.4.1 in combination with high magnifications can be used to mitigate optical cross talk. The spatial distribution of the  $\overline{SNR}$  from Eq. (1.16) and contributions to the mean photon numbers for a low and high magnification scenario are used as illustrations. I conclude that the readout is limited by cross talk for low magnifications, while it is limited by CIC noise at high magnifications.

The top part of Fig. 4.1a and 4.1b shows the  $\overline{SNR}$  defined in Eq. (4.1) for low and high magnification scenarios. The  $\overline{SNR}$  is best for pixels close to the middle ion. The worst pixels are where the neighboring ions have their center. In between, an interference pattern created by the sum of the three Airy functions from Eq. (1.3) can be observed.

The bottom part of Fig. 4.1a and 4.1b shows the continuous spatial distribution of the mean photon numbers for the ion signal and background. The ion under investigation is in the middle in light blue, the shape of its distribution is given by the Airy function in Eq. (1.3). The background is

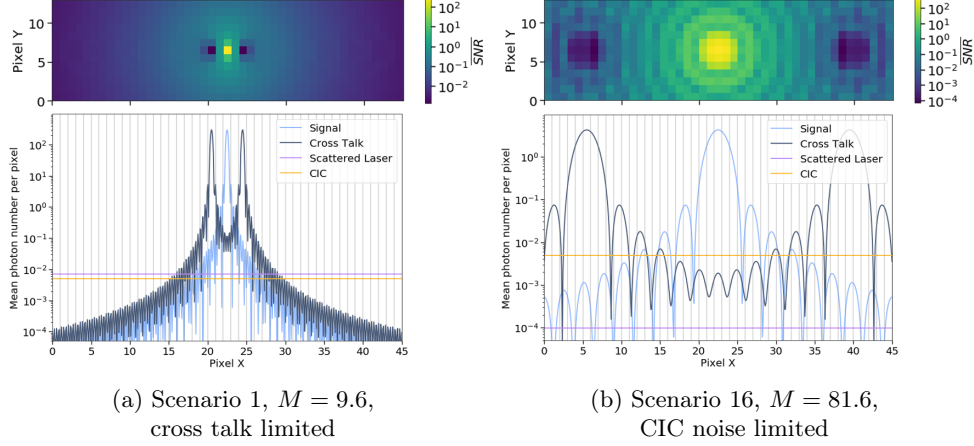


Figure 4.1: Spatial distribution of  $\overline{SNR}$  (top) and contributions to the mean photon number (bottom) for scenario 1 and 16. The bottom plot shows the continuous spatial distribution of the mean photon numbers for a horizontal cross section through the middle of the top plot.

split up into scattered laser light, cross talk and CIC. There are two neighboring ions that contribute to the optical cross talk, their shape is again the Airy function. The photon numbers are normalized by the pixel area. To obtain the mean number of photons incident on a pixel, the integral between the gray vertical lines has to be taken. The plots correspond to a horizontal cross section through the  $\overline{SNR}$  plots above, where the  $\overline{SNR}$  has been calculated from the different contributions. For our experimental parameters, the contribution of scattered laser light can be neglected. The optical cross talk per pixel decreases for higher magnifications, since the signals of the neighboring ions are spread over more pixels. The gain in spatial information makes more pixels with a high ion signal but little cross talk available.

The CIC per pixel is independent of the magnification. The limiting factor per pixel for the  $\overline{SNR}$  and the readout fidelity thus changes from optical cross talk at low magnifications to CIC noise at high magnifications. The effect of optical cross talk can be mitigated at high magnifications. The change of limit is also visible in the  $\overline{SNR}$  plot. For the CIC limit, the best  $\overline{SNR}$  pixels are spread symmetrically around the middle ion, while for the cross talk limit, pixels at the top and bottom of the middle ion are preferred.

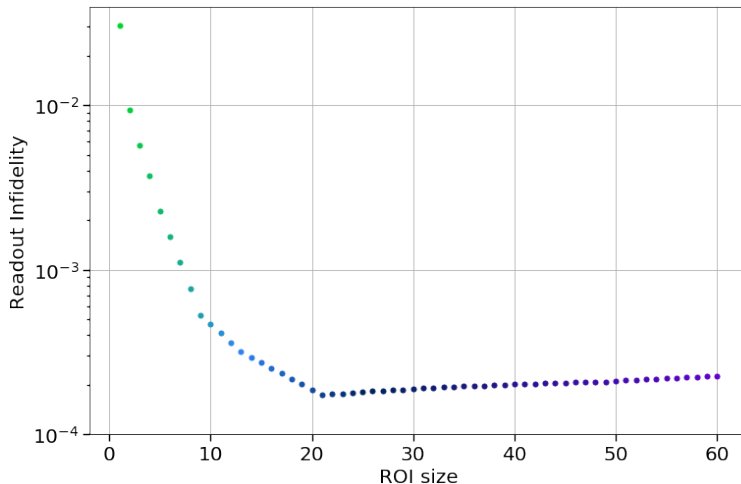


Figure 4.2: Readout infidelity of scenario 16 for increasing ROI size. The ROI size corresponds to the number of pixels in the ROI  $N$  considered for digital binning. The  $N$  best pixels are picked according to their  $\overline{SNR}$  seen in Fig. 4.1b. The optimal number of pixels is at  $N_{\text{ROI}}^{16} = 21$ . The ROI size is also mirrored in the color of the points for later reference.

### 4.1.2 Magnification and ROI Size

In the following, I discuss the dependency of the readout fidelity on the number of pixels in the ROI and magnification. I conclude that there is an optimal ROI size for each magnification, and that low readout infidelities can be achieved for both low and high magnification scenarios.

For scenario 16, the readout fidelity for increasing ROI size is shown in Fig. 4.2. For each point, the  $N$  best pixels are picked according to their  $\overline{SNR}$  value, where  $N$  is the number of pixels in the ROI.

For higher magnifications, the ion signal is spread across many pixels. By increasing the ROI, more signal is collected, increasing the fidelity. However, pixels also have a decreasing  $\overline{SNR}$  due to optical cross talk and CIC. At some point, these negative contributions overweight the gain in signal. There is an optimal value  $N_{\text{ROI}}^p$  depending on the scenario that minimizes the readout infidelity. Since this scenario is CIC limited, the increase in background photons is linear with  $N$ , resulting in a continuous increase in infidelity for high  $N$ . The exact dependence varies for different scenarios, but all have an optimal ROI size that minimizes infidelity.

Figure 4.3 shows the readout infidelity for scalable scenarios with increas-

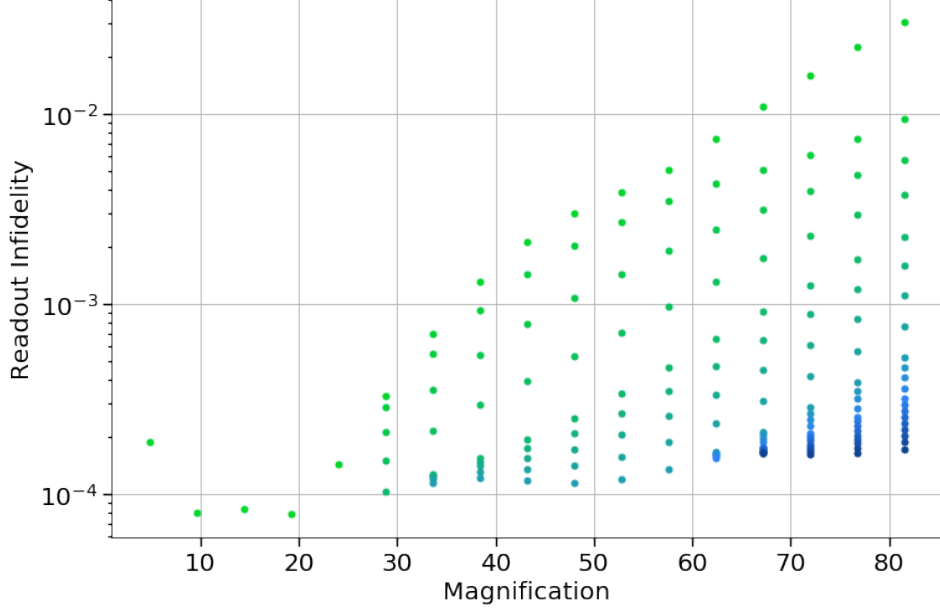


Figure 4.3: Readout infidelity for increasing magnification. The fidelity is only evaluated for scalable scenarios with  $M_p$ ,  $p \in [0, 16]$ .  $p = 0$  is the second point from the left,  $p = 16$  the last point on the right. For each scenario, the readout fidelity is calculated for multiple ROI sizes. The points follow Fig. 4.2 and use the same color code. The ROI is increased until the optimum  $N_{\text{ROI}}^p$  is reached. This means the ROI size and readout fidelity increases from top to bottom.

ing magnification. For each scenario, increasing ROI sizes are plotted (from top to bottom) until the optimal readout fidelity is reached.

The optimal number of pixels in the ROI  $N_{\text{ROI}}^p$  is higher for increasing magnification. For low magnifications, it is only a single pixel, since the  $\overline{SNR}$  drops quickly due to the low spatial resolution. Starting from scenario 4, there is enough spatial resolution available such that binning multiple pixels increases fidelity. For higher magnifications, a larger ROI is required to compensate for the spread of the ion signal.

As discussed in Section 4.1.1, optical cross talk is mitigated for increasing magnifications. The system changes from the cross talk limit to the CIC limit. For our particular ion spacing and Airy disk radius, the optical cross talk is small compared to the CIC. Therefore, low magnifications generally produce better readout infidelities, with an optimum below  $10^{-4}$  for scenario

1 with ROI size 1. The lowest infidelity for the high magnification scenario at  $M = 81$  is around twice as large.

It is not beneficial to go to even higher magnifications due to the CIC limit. The CIC increases linearly with  $N_{\text{ROI}}^p$ . For large ROI this decreases the lowest possible infidelity.

There are small variations in the lowest possible infidelities depending on magnification. They can be explained by the discretization of the continuous spatial distribution from Fig. 4.1 over the pixel raster. For particular magnifications, pixels line up with the Airy fringes of the ion signal, resulting in a higher  $\overline{SNR}$  per pixel and a better lowest readout infidelity.

For a certain magnification, the sensor width is limiting the number of ions in a chain the camera can read out. The higher the magnification, the less ions fit on the sensor. For scalable scenarios with magnification  $M_p$ , the maximum number of ions is given by

$$N_{\text{ion}} \leq \frac{P_x W}{M_p d}, \quad (4.2)$$

where  $P_x$  is the pixel size,  $W$  the number of pixels and  $d$  the ion separation. For the Nuvu at full pixel width, the chain can contain 7 ions at high magnification (scenario 16 at  $M = 81.6$ ), and 60 ions at low magnification (scenario 1 at  $M = 9.6$ ).

### 4.1.3 Ion Position Shift

So far, it was always assumed that the ions are centered in the middle of pixels. In an experiment however, we have to deal with limited precision in alignment of the camera with respect to the trapped ions or ion drifts over time. In the following, I discuss the sensitivity of the readout fidelity to such ion position shifts. Simulated is a horizontal shift of the whole ion chain in the object plane, which means it is magnified by  $M$  in the image plane.

For **pre-calibration** position shifts, the ROI can still be calibrated to account for the misalignment. This sensitivity tells us how precise the camera has to be aligned with respect to the trapped ions to achieve a certain readout fidelity. The effect of a horizontal ion shift on the readout fidelity is shown in Fig. 4.4. Once the ions are shifted by a full pixel width in the image plane, the pattern repeats. Hence, the ion shift is periodic with period proportional to  $1/M$  in the object plane.

High magnifications (blue) manage to retain the same level of fidelity for arbitrary ion shifts. The reason being that more spatial resolution is available to compensate the shift with an adjusted ROI, which is independent of cross

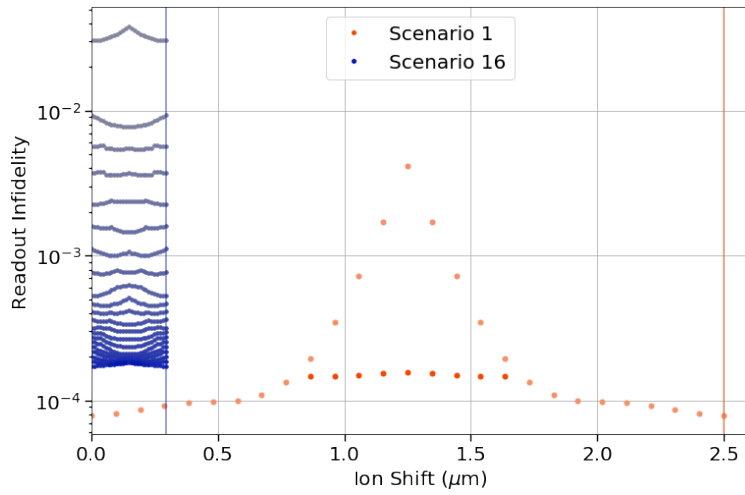


Figure 4.4: Readout infidelity for a horizontal shift of the ion chain before calibration. For each shift, the infidelity is plotted for an increasing number of pixels in the ROI from top to bottom until  $N_{\text{ROI}}^p$  is reached. The shift is with respect to the optimal ion positions in the center of pixels and plotted for the object plane. Vertical lines correspond to a pixel width in the image plane. The pattern repeat after the vertical lines.

talk since the system is CIC limited. They are robust to pre-calibration ion shifts and can achieve similar performance independent of the camera alignment. Low magnifications (orange) are more sensitive to ion shifts in the pre-calibration phase. They lack spatial resolution and are cross talk limited. By expanding the ROI from one to two pixels to collect the ion signal, inevitably more cross talk is picked up, reducing the fidelity.

Since we have little cross talk in our system, low magnifications have a better fidelity for perfect alignment, and still have a relatively high fidelity for the worst case when the ion center is between pixels. High magnifications suffer from the CIC limit, which gives them a lower fidelity to start with. For these two scenarios, choosing higher magnifications seems not beneficial. However, for different experimental parameters or an intermediate magnification, the initial loss in fidelity is lower while still maintaining a better variance. Depending on the given precision, it is more suitable than the low magnification scenario.

For **post-calibration** shifts, the ROI is already calibrated and stays fixed. This sensitivity is relevant when ions drift during an experiment or are inaccurately transported before readout. Figure 4.5 shows the readout fidelity for an ion shift after the calibration. Both scenario 1 and 16 have been calibrated for the optimal position at zero shift. The problem is completely symmetric, so shifts can be to the left or right along the horizontal axis.

High magnifications (blue) are more sensitive to ion shifts after calibration. The equivalent pixel width in the object plane is small, since the shifts are significantly magnified. This means the ions are shifted by many pixels, putting them outside of the optimal ROI and reducing the readout fidelity. Since the ROI is large, shifting the ion by an equivalent pixel width only leaves a fraction of the ROI misaligned and does not reduce the fidelity strongly. However, this effect is mitigated by the high magnification which enhances the shift, resulting in the high position sensitivity. Low magnifications (orange) are more robust against ion shifts after calibration. The equivalent pixel width in the object plane is large, which protects the readout fidelity. The ions are shifted across the pixels more slowly, leaving them inside the single pixel ROI longer. When shifting the ion image by a quarter of the equivalent pixel width, the readout fidelity is completely preserved. Once the ion is shifted more than half a pixel, more signal lies outside of the ROI than inside, and the readout fidelity decreases strongly. For ion shifts of more than a few  $\mu\text{m}$ , the readout fidelity collapses for both scenarios and a recalibration before readout is required.

I conclude that high magnification scenarios are less sensitive to position shifts pre-calibration, but more sensitive once the calibration is done. For

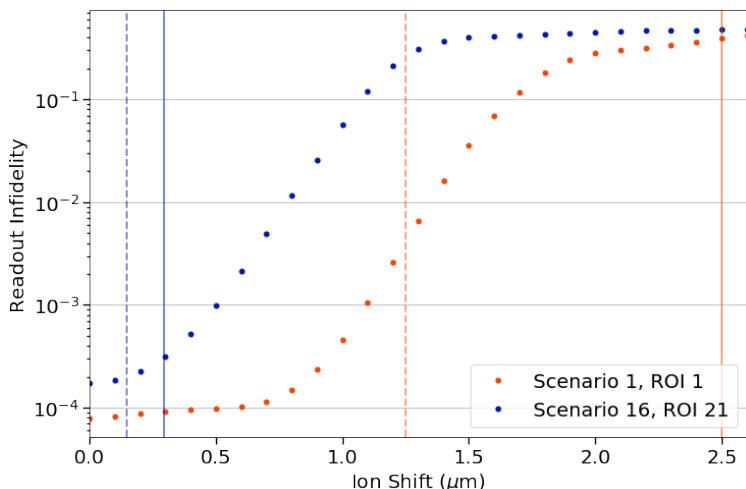


Figure 4.5: Readout infidelity for a horizontal shift of the ion chain after calibration. The ROI has been calibrated at zero shift where the ions are in the center of the pixels. Plotted is the shift in the object plane. Solid vertical lines correspond to a full pixel width in the image plane, vertical dotted lines to half the width.

low magnification scenarios, it is the other way round. Depending on how good precisions are in a system, a magnification can be chosen that is most robust against the limiting shifts. If both pre- and post-calibration precision are limiting, an intermediate magnification might be the best compromise.

#### 4.1.4 Ion States and Threshold

The optical cross talk introduces a nearest neighbor state-dependency of the readout fidelity and optimal threshold. In the following, I investigate the readout fidelity for all possible neighboring states and miscalibrated thresholds.

The readout infidelity is plotted for all four possible neighboring states at different thresholds in Fig. 4.6. When both neighboring ions are bright, the optimal readout fidelity is worst since the amount of cross talk is highest. For only one of the neighboring ions bright, the best possible readout infidelity decreases. This case also represents ions at the edge of a chain, which have better readout fidelity than ions in the middle of a chain. For both neighboring ions dark, the optimal readout fidelity is best due to the absence of optical cross talk in the background signal.

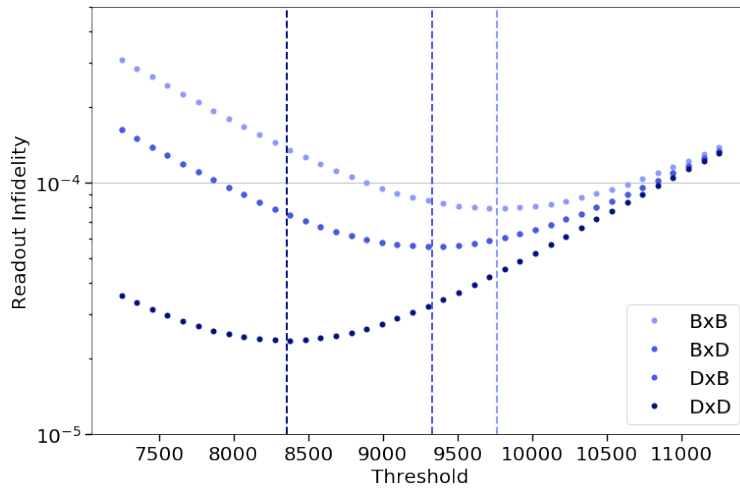


Figure 4.6: Readout infidelity depending on threshold and states of neighboring ions for scenario 1 with ROI 1. Neighboring dark states are denoted by “D” and bright states by “B”. The state of the middle ion is unknown “x”. The optimal threshold at the minimum of the readout infidelity is marked by dotted vertical lines for each state. “BxD” and “DxB” have the exact same infidelity, since the scalable scenarios are completely symmetric.

Since our system has little cross talk, the optimal thresholds are close, even for cross talk limited low magnifications. None of the state curves intersect, which enables us to select a fixed threshold with low infidelities for all states. We decide to calibrate our device for the case where all neighbors are bright and take the optimal threshold for this case as fixed. This means we optimize the worst readout fidelity and sit at the minimum of the “BxB” curve. All other states still have better fidelity even though the fixed threshold is non-optimal for them. When we do so for each ion in a chain, it allows us to quantify a lower bound for the overall readout fidelity.

With a more advanced thresholding algorithm that iteratively adjust thresholds depending on ion states, the average readout fidelity over all states could be further improved. This corresponds to the “Iterative Threshold Method” in [13]. As a result, instead of the average over the infidelities for the fixed “BxB” threshold, the average would be taken over all the minimal infidelities in Fig 4.6. The worst case fidelity is not reduced, and efforts to optimize it are still relevant for adaptive algorithms in the same setup.

#### 4.1.5 Exposure Time

The exposure time is the most critical parameter, since it influences both readout fidelity and state discrimination time. Here I simulate the dependence of the readout fidelity on exposure time. A shorter exposure time reduces state discrimination time, but decreases readout fidelity. A more sensitive detector and a diffraction limited lens can reduce exposure times while maintaining similar readout fidelities.

As an example, Fig. 4.7 shows the readout infidelity that can be achieved for varying exposure time with scenario 1 at ROI 1.

Since the rate of signal photons is larger than the rate of background photons, a longer exposure time linearly separates the bright and dark state photon numbers in Eq. (3.5) and (3.4). This decreases the readout infidelity exponentially since the tails of the bright and dark state distribution drop off exponentially. In this simulation, I assume ideal qubits with no spontaneous decay. For short state discrimination times, this is a good approximation. For longer exposure times, a limited qubit lifetime increases the infidelity due to spontaneous decay during the exposure.

Since in Eq. (3.5) and (3.4) the exposure time is always scaled by  $\eta$  and  $Q$ , a more sensitive detector or lens with higher collection efficiency have the same effect as a longer exposure time. Therefore, the more sensitive version of the Nuvu with  $Q = 90\%$  could achieve the same readout fidelities with half the exposure time. Replacing the Schwarzschild-type objective

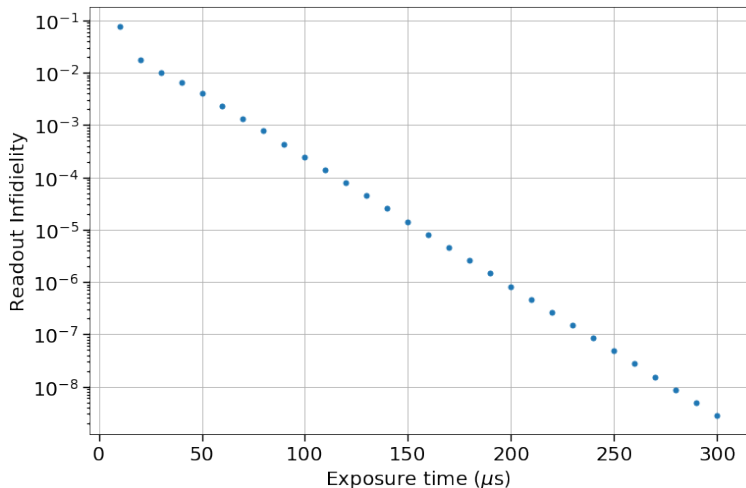


Figure 4.7: Readout infidelity for varying exposure times. This particular case is scenario 1 with ROI 1. The quantum efficiency of the camera is  $Q = 45\%$ .

with an ideal diffraction limited lens with  $NA = 0.5$  would increase the detection efficiency, but also reduce optical cross talk further. Infidelities of  $10^{-4}$  could then be reached with  $45 \mu\text{s}$  exposure time. Combining these two options,  $10^{-4}$  readout infidelities could be achieved with exposure times as low as  $22 \mu\text{s}$ .

## 4.2 State Discrimination Time

A fundamental limit for quantum computation is given by the finite life and coherence times of qubits [15]. To circumvent this limit for quantum algorithms which use measurement-based feedback, e.g. QEC codes [2, 3], feedback and thus readout duration needs to be small compared to the relevant decay or decoherence time scales. Additionally, fast feedback enables short computational times and faster data acquisition. In this section, I calculate the state discrimination time defined in Eq. (3.7) as a measure of readout duration. In our readout device, the main contributions are the exposure with  $120 \mu\text{s}$  and camera readout time with  $105 \mu\text{s}$ . The model for the readout time of a FT EMCCD camera is validated with a measurement of the *Andor iXon 888* camera. The relevant details for both cameras are given in Table 4.3. I conclude that we expect to achieve state discrimination

Table 4.3: Relevant parameters for the calculation of the camera readout time for the Andor and Nuvu camera. Both cameras are Frame Transfer (FT) EMCCDs. They use a similar sensor made by the same manufacturer.

<b>Camera</b>	<i>Nuvu HNU 128 AO</i>	<i>Andor iXon 888</i>
Sensor	<i>E2V CCD60<sup>a</sup></i>	<i>E2V CCD201<sup>b</sup></i>
Vertical shift freq. (MHz)	10	1.66
Horizontal shift freq. (MHz)	20	30
Camera Link freq. (MHz)	20	60
Storage area height (px)	132	1039
Storage delay ( $\mu\text{s}$ )	29.4 <sup>*</sup>	20.4 <sup>*</sup>
Vertical shift time ( $\mu\text{s}$ )	0.2 <sup>*</sup>	1.2 <sup>*</sup>
No. of gain registers	512	604
No. of dummy registers	24	468
No. of overscan registers	8	32

<sup>a</sup> [https://www.e2v.com/shared/content/resources/File/documents/Imaging%202017/EM%20Sensors/CCD60/a1a-ccd60\\_bi\\_5\\_v1.pdf](https://www.e2v.com/shared/content/resources/File/documents/Imaging%202017/EM%20Sensors/CCD60/a1a-ccd60_bi_5_v1.pdf)

<sup>b</sup> <https://www.e2v.com/resources/account/download-datasheet/1491>

<sup>\*</sup> Estimation based on sensor data sheet.

times of 225  $\mu\text{s}$  for readout infidelities of  $10^{-4}$  in our setup.

The state analysis time from Eq. (2.2) is  $t_{\text{analysis}} = 100 \text{ ns}$  using our real time FPGA implementation of the state discrimination protocol. The state transfer time in our case is given by Eq. (2.1) and is  $t_{\text{transfer}} = 650 \text{ ns}$  for 10 ions<sup>1</sup>. The exposure time is determined by the desired readout fidelity. For scenario 1 with ROI 1 simulated in Section 4.1, it is  $t_{\text{exp}} = 120 \mu\text{s}$  for a readout infidelity just below  $10^{-4}$ .

The camera readout time defined in Eq. (1.11) depends on the cropped frame height and width. Minimizing the cropped frame dimensions to tightly envelop the ROI from calibration minimizes the camera readout time. The required height and width depend on the magnification and length of the ion chain. High magnifications or long ion chains require frames with large width. Figure 4.8 shows the camera readout time for the full width of the Nuvu camera (128 pixels) for different frame heights. The slope given by

<sup>1</sup>For more ions, the state transfer time can be speed up by a higher transmitter clock frequency, see Subsection 2.3.2.

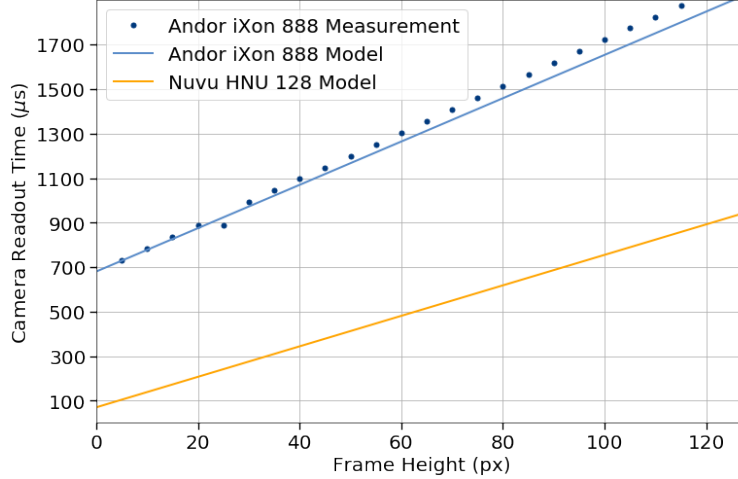


Figure 4.8: Camera readout time for different cropped frame heights at constant frame width of 128 pixels. Plotted are the values obtained from Eq. (1.11) with parameters from Table 4.3 for the Andor and Nuvu (lines). The Andor readout is limited in width by Eq. (4.4). Shown are also measured values for the Andor (dots).

Eq. (1.12) is steep since reading out one more line requires shifting a full width of pixels  $W$  from the image area to the ADC. The offset is given by

$$t_{\text{read}}(0, 0) = t_S + \frac{1}{f_v} S_Y + \frac{1}{f_h} (N_D + N_G) . \quad (4.3)$$

The readout times of the Andor are long compared to the Nuvu. The offset is increased due to the larger storage area  $S_Y$  with lower vertical shift frequency  $f_v$  and more dummy registers  $N_D$ . The slope is steeper since the Andor is restricted to frame widths (plus overscan) that are power of two

$$W' = 2^{\lceil \log_2(W+N_O) \rceil} . \quad (4.4)$$

The actual frame width shifted to the ADC in this case is  $W' = 256$ . The measurement was performed with the “Latency Measurement” core on the FPGA described in Section 2.3.1. The values obtained from Eq. (1.11) agree well with the measurements for small heights. For increasing heights, the predicted and measured values start to drift apart, indicating that the estimated vertical shift time  $t_{\text{vshift}}$  in the slope is slightly off. For readout of linear ion chains at high magnifications, no more than 5 lines are needed,

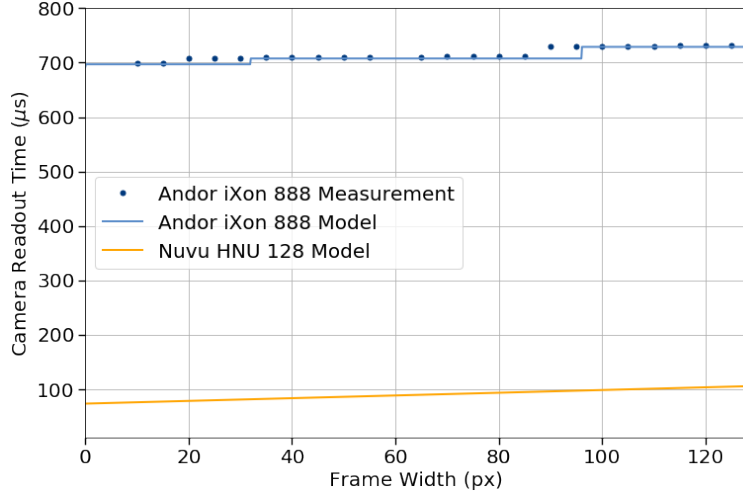


Figure 4.9: Camera readout time for different cropped frame widths at constant frame height of 5 pixels. Plotted are the values obtained from Eq. (1.11) with parameters from Table 4.3 for the Andor and Nuvu (lines). The Andor readout is limited in width by Eq. (4.4). Shown are also measured values for the Andor (dots).

see for example scenario 16 with ROI 21 in Fig. 4.1b. I estimate that the Nuvu can achieve this in around 100  $\mu\text{s}$ .

Low magnifications or shorter ion chains require less frame width. Figure 4.9 shows the camera readout time at constant frame height of 5 pixel for varying cropped frame widths. By not reading out the full width of the sensor, the camera readout time can in principle be reduced. Since the height  $H$  is small in our case, the slope given by Eq. (1.13) is insignificant.

Again, the Andor readout is slower due to a larger offset. Jumps in the Andor measurement express a readout limitation in width. However, the predicted jumps from Eq. (4.4) do not line up with the measurement. The reason for this is unclear. In the plateaus, the model and measurement agree well again. For the Nuvu, not reading out the full width provides small time gains, enabling readout times below 100  $\mu\text{s}$ . Reading out the full width at  $5 \times 128$  on the Nuvu takes around

$$t_{\text{read}}(5, 128) \approx 105 \mu\text{s} . \quad (4.5)$$

I now discuss the contributions to the camera readout time for the Nuvu. In Fig. 4.10, the individual contributions are plotted for a  $5 \times 128$  cropped

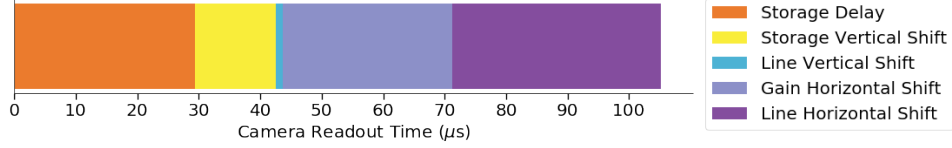


Figure 4.10: Contributions to the camera readout time for the Nuvu camera at a cropped frame of size  $5 \times 128$ . The total camera readout time is  $105 \mu\text{s}$ . The contributions are explained in the main text. This plot is not a timing diagram, since the times for the sequential line readout are summed up.

frame. Shown are delay before starting the storage shift  $t_S$ , vertical shift through the storage area  $\frac{1}{f_v} S_Y$ , vertical shift during line readout  $H t_{\text{vshift}}$ , horizontal shift through dummy and gain registers  $\frac{1}{f_h} (N_D + N_G)$  and horizontal shifts during line readout  $H(W + N_O) \frac{1}{f_h}$ . Only the contributions of the line readout scale with the cropped frame size, the others are constant offsets.

Since only few lines are read out, line vertical shifts make up only a small part of the readout time. All other processes significantly contribute to the camera readout time. With a new sensor combining current technologies, the readout time might potentially be reduced. By using a smaller  $5 \times 128$  FT EMCCD, the storage vertical shift is speed up since the storage area is smaller. The storage delay can be cut down by optimizing timings, similar to the Andor. The horizontal shift could be accelerated to the same speed as the Andor. Altogether, this could lower the readout time to  $\approx 50 \mu\text{s}$ .

I conclude that in our case, the state analysis and transfer time are sub  $\mu\text{s}$ . The state discrimination time is dominated by the exposure and camera readout time. With our setup, see Table 4.1, I estimate

$$t_{\text{disc}} \approx 225 \mu\text{s} \quad (4.6)$$

for a frame size of  $5 \times 128$ . This enables parallel readout of 7 to 60 ions in chain with infidelities on the order of  $10^{-4}$ , see Section 4.1.2. Combining the sensor optimized for fast readout with high quantum efficiency and an ideal lens, see Section 4.1.5, one could achieve state discrimination times around  $72 \mu\text{s}$  with infidelities of  $10^{-4}$ .

### 4.3 Detector Comparison

In this section, I compare state-of-the-art EMCCD, CMOS and multi-channel PMT detectors and evaluate their performance for low-latency and high-fidelity parallel readout of ion chains. This allows us to assess the use of commercially available cameras for parallel ion readout in our setup. As introduced in Section 1.3, multi-channel PMTs have already been used for low-latency parallel readout [4, 12]. EMCCD cameras have been used for high-fidelity parallel readout with slow image post-processing [13, 14], while CMOS cameras represent a promising candidate for low-latency readout due to potentially faster camera readout. As a summary, I give pros and cons and conclude why we choose an EMCCD camera as a novel approach for providing low-latency readout in a fast feedback system.

As an example, scenario 1 with ROI 1 from Section 4.1 is used for the comparison. It is assumed that a similar spatial distribution can be achieved for all detectors by adjusting the magnification to compensate for different sensor sizes. The mean photon numbers for the CMOS and PMT are obtained from the EMCCD values. The CIC noise is subtracted and the different quantum efficiencies are accounted for. For the multi-channel PMT, alternating channels are used to image the ions, like in [12]. The electronic cross talk generally depends on next-nearest neighbors via optical cross talk. It is approximated by adding  $2 \times 0.6\%$  of the bright photon number from the nearest neighbors to both dark and bright state. This approximation is good, since cross talk is small compared to the neighboring ion signal. In scenario 1, the electronic cross talk is of the same order of magnitude as the optical one. To match the high count values of the EMCCD, the CMOS and PMT counts are multiplied by a factor

$$\beta' = \frac{\beta}{G}, \quad (4.7)$$

where  $\beta$  is the conversion factor and  $G$  the EM gain of the EMCCD. They are also shifted by the EMCCD offset  $\mu$ . These operations leave the overlap between dark and bright state invariant.

Figure 4.11 shows the dark and bright state distribution for the three different sensor types. The different limitations of the detectors are visible in the shape and tails of the count distributions: The PMT is shot noise limited, but has an increased dark state photon number due to electronic cross talk. Still, the dark state tail drops off fast. The bright state photon number however suffers from a low quantum efficiency. This results in a reduced state separation between dark and bright and an increased overlap.

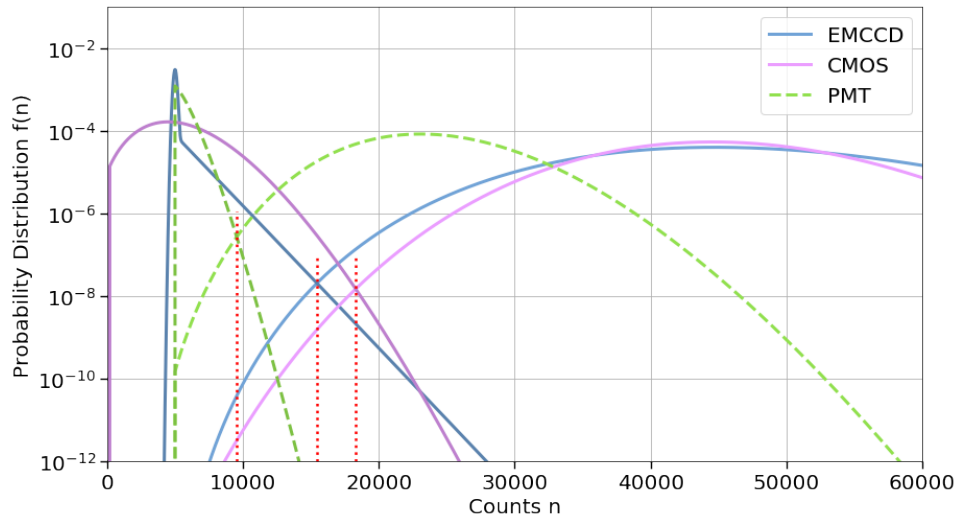


Figure 4.11: Comparison between EMCCD, CMOS and multi-channel PMT. Shown is the bright and dark state distribution for scenario 1 with ROI 1 and the corresponding optimal threshold (red vertical line). Unlike other simulations, the EMCCD has enhanced quantum efficiency  $Q = 90\%$ . The exposure time is reduced to  $t_{\text{exp}} = 70 \mu\text{s}$ . The details and mean photon numbers for each detector can be found in Table 4.2.

Sensor	Advantage	Disadvantage
Multi-channel PMT	<ul style="list-style-type: none"> <li>➤ Low latency</li> <li>➤ Shot noise limited</li> <li>➤ Simple interface</li> </ul>	<ul style="list-style-type: none"> <li>➤ Low quantum efficiency</li> <li>➤ Electronic cross-talk</li> <li>➤ Requires high magnification</li> </ul>
CMOS	<ul style="list-style-type: none"> <li>➤ High quantum efficiency</li> <li>➤ No analog bottleneck</li> <li>➤ Cheap</li> </ul>	<ul style="list-style-type: none"> <li>➤ Readout noise</li> <li>➤ Low pixel uniformity</li> <li>➤ Requires low magnification</li> </ul>
EMCCD	<ul style="list-style-type: none"> <li>➤ High quantum efficiency</li> <li>➤ Negligible readout noise</li> <li>➤ Flexibility with binning</li> <li>➤ High pixel uniformity</li> </ul>	<ul style="list-style-type: none"> <li>➤ Excess noise</li> <li>➤ CIC noise</li> <li>➤ Analog bottleneck</li> <li>➤ Expensive</li> </ul>

Figure 4.12: Summary of different sensor technologies for parallel ion read-out. Presented are the pros and cons of state-of-the-art EMCCD, CMOS and multi-channel PMTs.

The EMCCD is excess noise limited. It is similar to the shot noise limit with an additional noise factor introduced by the probabilistic gain mechanism. The dark state tail is less steep than the PMT one, and the bright state distribution is broadened, reducing the readout fidelity. The CMOS is readout noise limited, showing a broad dark state distribution. The bright state distribution is not affected by the high readout noise. The uncertainty for the dark state increases the overlap. The EMCCD and CMOS have similar readout infidelity below  $10^{-4}$ , while the PMT is an order of magnitude higher. The comparison between sensors is summarized in Fig. 4.12.

The CMOS camera used for this comparison represents a family of cameras with high UV sensitivity that are promising candidates for ion read out. At the time of writing, the available models however do not have a Camera Link interface and are thus not suitable for low-latency readout. The readout fidelities for CMOS cameras reduce drastically as we go to higher magnifications since readout noise is added in digital binning. Only low magnification scenarios are feasible and require high precision in alignment. These scenarios are always prone to cross talk and require optimized optical setups. CMOS systems are less scalable since the pixel uniformity is low. Finding good pixels with little readout in a row might be hard, and changes from sensor to sensor. Even though CMOS readout can in principle be faster due to its architecture, camera readout times have not been measured or verified, partly due to lack of Camera Link. Still, CMOS are close in performance to EMCCDs for certain scenarios. CMOS with high quantum efficiencies,

lower readout noise and better pixel uniformity might be an option for fast parallel ion readout in the future.

Multi-channel PMTs require very high magnifications due to the large sensor size. This makes imaging of long ion chains problematic. Even though they are shot noise limited, PMT technology is old and has limited quantum efficiency. The interface is simpler than Camera Link and readout times are negligible. The high time resolution can be used in state discrimination protocols to effectively reduce cross talk (electronic or optical). This can decrease readout infidelity by up to 30% compared to conventional thresholding [12]. In this case, an average readout infidelity over all possible states of  $10^{-2}$  is achieved in  $150 \mu\text{s}$ .

We choose an EMCCD for this project for the following reasons: Low readout noise and high pixel uniformity offer a high flexibility since both low and high magnifications scenarios are supported. Optical cross talk can be reduced with high magnifications, which means EMCCD can work even in non-ideal setups. Due to the spatial resolution, camera readout is scalable to longer ion chains or larger ion crystals with low magnifications. Even though EMCCDs suffer from an analog bottleneck, readout times have been measured and suffice our requirements. Although EMCCDs have excess and CIC noise, they offer high quantum efficiencies and can achieve high-fidelity readout. In our case, the estimated readout infidelity is  $10^{-4}$  for state discrimination times of around  $225 \mu\text{s}$ .

# Summary and Outlook

In this work, I have evaluated the feasibility of integrating cameras into experiment control systems for low-latency and high-fidelity parallel readout of trapped ions. I have shown that using a commercially available EMCCD and performing fast image analysis on an FPGA, we expect to achieve parallel readout with an upper-bound readout infidelity of  $10^{-4}$  in  $225\ \mu\text{s}$  for up to 60 ions in a linear chain.

The readout device proposed in this work is developed as a standalone and can thus be easily integrated into existing experiment control systems. It is based on EMCCD sensors that offer higher sensitivity than PMTs and have negligible readout noise. Despite their excess noise, they can be used for high-fidelity readout that reaches the threshold for fault tolerant quantum computation. Digital binning, which is only limited by CIC noise, makes both low and high magnification scenarios possible. The spatial information gained from sensor arrays gives the ability to mitigate optical cross talk, which is necessary for non-optimized imaging systems. Our readout device offers a scalable solution that benefits from a substantial speed up thanks to parallel readout of multiple ions. The carefully selected *Nuvu HNU 128* camera has sufficiently fast sensor readout and allows for short exposure times due to its high sensitivity. We gain multiple orders of magnitude on processing time by using Camera Link and FPGAs for real time state analysis instead of post-processing images on a PC. This enables low-latency state detection and opens the path for cameras to be used in fast measurement-based feedback loops for QEC codes. Using the Camera Link standard guarantees that our device is future-proof, since it can also support improved camera models. Further, the FPGA hardware is scalable up to 400 ions with the current implementation.

The next step is to verify the simulation results in an experiment. For this, we require a setup that can trap three ions in a linear chain, control single ion states, and induce state-dependent fluorescence for all ions. By repeatedly preparing the ions in a known state and performing readout,

the readout fidelity can be measured. This experiment requires the implementation of some additional software features. Firstly, the state of the ions determined during image analysis has to be buffered on the FPGA and made accessible for analysis. Secondly, the calibration of the ROI and thresholds required for the state discrimination algorithm needs to be automated in a Python script.

This project can be extended by implementing the iterative thresholding method on the FPGA, which can improve the average readout fidelity over all ion states. Furthermore, more advanced state discrimination algorithms can be considered. Their performance needs to be evaluated and their feasibility for an FPGA implementation has to be assessed. For example, the spatial maximum likelihood method uses more spatial information to further mitigate cross talk and improve readout fidelity. With improved hardware, a faster state discrimination could be achieved while maintaining the high readout fidelity. Specifically, a diffraction-limited lens with a NA of 0.5, and a camera which has 90% quantum efficiency and is optimized for low-latency, could lower the state discrimination time to 72  $\mu\text{s}$ . A comparison between state-of-the-art EMCCD, CMOS and multi-channel PMT detectors points towards the fact that EMCCDs are currently the best option for low-latency and high-fidelity parallel readout of ions. Nevertheless, improved CMOS cameras might be good candidates for ion readout, since under specific conditions current CMOS already perform as well as EMCCDs. In particular, they should have a Camera Link interface, high quantum efficiency, reduced readout noise and a higher pixel uniformity. The tools developed in this project can be used to simulate such future cameras based on their specifications and compare them to existing solutions.

# Bibliography

- [1] M. A. Nielsen and I. L. Chuang, “Programmable Quantum Gate Arrays,” *PHYSICAL REVIEW LETTERS*, vol. 79, no. 2, p. 4, 1997.
- [2] P. W. Shor, “Scheme for reducing decoherence in quantum computer memory,” *Physical Review A*, vol. 52, pp. R2493–R2496, Oct. 1995.
- [3] A. Steane, “Multiple-particle interference and quantum error correction,” *Proceedings of the Royal Society of London. Series A: Mathematical, Physical and Engineering Sciences*, vol. 452, pp. 2551–2577, Nov. 1996.
- [4] S. Debnath, N. M. Linke, C. Figgatt, K. A. Landsman, K. Wright, and C. Monroe, “Demonstration of a small programmable quantum computer with atomic qubits,” *Nature*, vol. 536, pp. 63–66, Aug. 2016.
- [5] C. Hempel, C. Maier, J. Romero, J. McClean, T. Monz, H. Shen, P. Jurcevic, B. P. Lanyon, P. Love, R. Babbush, A. Aspuru-Guzik, R. Blatt, and C. F. Roos, “Quantum Chemistry Calculations on a Trapped-Ion Quantum Simulator,” *Physical Review X*, vol. 8, July 2018.
- [6] J. J. Bollinger, J. W. Britton, and B. C. Sawyer, “Quantum simulation and many-body physics with hundreds of trapped ions,” in *CLEO: 2013*, (San Jose, California), p. QTu3C.5, OSA, 2013.
- [7] C. Gross and I. Bloch, “Quantum simulations with ultracold atoms in optical lattices,” *Science*, vol. 357, pp. 995–1001, Sept. 2017.
- [8] E. Knill, “Quantum computing with realistically noisy devices,” *Nature*, vol. 434, pp. 39–44, Mar. 2005.
- [9] A. Bermudez, X. Xu, R. Nigmatullin, J. O’Gorman, V. Negnevitsky, P. Schindler, T. Monz, U. G. Poschinger, C. Hempel, J. Home, F. Schmidt-Kaler, M. Biercuk, R. Blatt, S. Benjamin, and M. Müller,

- “Assessing the Progress of Trapped-Ion Processors Towards Fault-Tolerant Quantum Computation,” *Physical Review X*, vol. 7, Dec. 2017.
- [10] V. Negnevitsky, M. Marinelli, K. Mehta, H.-Y. Lo, C. Flühmann, and J. P. Home, “Repeated multi-qubit readout and feedback with a mixed-species trapped-ion register,” *arXiv:1804.09703 [physics, physics:quant-ph]*, Apr. 2018.
- [11] A. H. Myerson, D. J. Szwer, S. C. Webster, D. T. C. Allcock, M. J. Curtis, G. Imreh, J. A. Sherman, D. N. Stacey, A. M. Steane, and D. M. Lucas, “High-Fidelity Readout of Trapped-Ion Qubits,” *Physical Review Letters*, vol. 100, May 2008.
- [12] A. Seif, K. A. Landsman, N. M. Linke, C. Figgatt, C. Monroe, and M. Hafezi, “Machine learning assisted readout of trapped-ion qubits,” *Journal of Physics B: Atomic, Molecular and Optical Physics*, vol. 51, p. 174006, Sept. 2018.
- [13] A. H. Burrell, *High Fidelity Readout of Trapped Ion Qubits*. PhD thesis, Oxford, 2010.
- [14] A. H. Burrell, D. J. Szwer, S. C. Webster, and D. M. Lucas, “Scalable simultaneous multi-qubit readout with 99.99% single-shot fidelity,” *Physical Review A*, vol. 81, Apr. 2010.
- [15] S. Haroche and J.-M. Raimond, *Exploring the Quantum: Atoms, Cavities, and Photons*. Oxford University Press, Aug. 2006.
- [16] V. Negnevitsky, *Feedback-Stabilised Quantum States in a Mixed-Species Ion System*. PhD thesis, 2018.
- [17] F. Leupold, *Bang-Bang Control of a Trapped-Ion Oscillator*. PhD thesis, 2015.
- [18] H. Haffner, C. Roos, and R. Blatt, “Quantum computing with trapped ions,” *Physics Reports*, vol. 469, pp. 155–203, Dec. 2008.
- [19] C. Donald, *Development of an Ion Trap Quantum Information Processor*. PhD thesis, Oxford, 2000.
- [20] E. Hecht, *Optics*. Addison Wesley, 2002.
- [21] P. Jerram, P. J. Pool, R. Bell, D. J. Burt, S. Bowring, S. Spencer, M. Hazelwood, I. Moody, N. Catlett, and P. S. Heyes, “The LLCCD:

- Low-light imaging without the need for an intensifier,” in *Photonics West 2001 - Electronic Imaging* (M. M. Blouke, J. Canosa, and N. Sampat, eds.), (San Jose, CA), p. 178, May 2001.
- [22] M. Hirsch, R. J. Wareham, M. L. Martin-Fernandez, M. P. Hobson, and D. J. Rolfe, “A Stochastic Model for Electron Multiplication Charge-Coupled Devices – From Theory to Practice,” *PLoS ONE*, vol. 8, p. e53671, Jan. 2013.
- [23] M. Loève, *Probability Theory. 1: ...* No. 45 in Graduate texts in mathematics, New York: Springer, 4. ed ed., 1977. OCLC: 310756077.
- [24] J. P. Crooks, S. E. Bohndiek, C. D. Arvanitis, R. Speller, H. XingLiang, E. G. Villani, M. Towrie, and R. Turchetta, “A CMOS Image Sensor With In-Pixel ADC, Timestamp, and Sparse Readout,” *IEEE Sensors Journal*, vol. 9, pp. 20–28, Jan. 2009.
- [25] N. Dutton, I. Gyongy, L. Parmesan, and R. Henderson, “Single Photon Counting Performance and Noise Analysis of CMOS SPAD-Based Image Sensors,” *Sensors*, vol. 16, p. 1122, July 2016.
- [26] B. Fowler, D. McGrath, and P. Bartkovjak, “Read Noise Distribution Modeling for CMOS Image Sensors,” p. 4, 2013.
- [27] L. Lindegren, “A general Maximum-Likelihood algorithm for model fitting to CCD sample data,” 2008.
- [28] AIA, “Global Machine Vision Interface Standards,” 2016.
- [29] R. Photonics, “CAMERA INTERFACES AND COMPUTER REQUIREMENTS,” *Northern Ireland*, no. 906, p. 4, 2017.
- [30] M-Labs, “ARTIQ: Advanced Real Time Infrastructure for Quantum Physics.” <http://m-labs.hk/artiq/>, 2018.
- [31] G. Kasprowicz, “Sinara Grabber Camera Interface.” <https://github.com/sinara-hw/Grabber>, Aug. 2018.



Eidgenössische Technische Hochschule Zürich  
Swiss Federal Institute of Technology Zurich

## Declaration of originality

The signed declaration of originality is a component of every semester paper, Bachelor's thesis, Master's thesis and any other degree paper undertaken during the course of studies, including the respective electronic versions.

Lecturers may also require a declaration of originality for other written papers compiled for their courses.

I hereby confirm that I am the sole author of the written work here enclosed and that I have compiled it in my own words. Parts excepted are corrections of form and content by the supervisor.

**Title of work** (in block letters):

Towards Low-Latency Parallel Readout of Multiple Trapped Ions

**Authored by** (in block letters):

*For papers written by groups the names of all authors are required.*

**Name(s):**

Schwegler

**First name(s):**

Nick

With my signature I confirm that

- I have committed none of the forms of plagiarism described in the ['Citation etiquette'](#) information sheet.
- I have documented all methods, data and processes truthfully.
- I have not manipulated any data.
- I have mentioned all persons who were significant facilitators of the work.

I am aware that the work may be screened electronically for plagiarism.

**Place, date**

Zürich, 16.10.18

**Signature(s)**

Nick Schwegler

*For papers written by groups the names of all authors are required. Their signatures collectively guarantee the entire content of the written paper.*